

Dynamics-oriented diagnostics for the Madden-Julian Oscillation

Bin Wang^{1,2}, Sun-Seon Lee³, Duane E. Waliser^{4, 5}, Chidong Zhang⁶, Adam Sobel⁷, Eric Maloney⁸, Tim Li^{1,2}, Xianan Jiang^{4,5}, and Kyung-Ja Ha⁹

¹ Department of Atmospheric Sciences and International Pacific Research Center, University of Hawaii, Honolulu, Hawaii 96822, USA

² Earth System Modeling Center, Nanjing University of Information Science and Technology, Nanjing, China

³ IBS Center for Climate Physics, Pusan National University, Busan, Korea

⁴ Joint Institute for Regional Earth System Science and Engineering, University of California, Los Angeles, California, USA

⁵ Jet Propulsion Laboratory, California Institute of Technology, Pasadena, California, USA

⁶ Pacific Marine Environmental Laboratory, National Oceanic and Atmospheric Administration, USA

⁷ Department of Applied Physics and Applied Mathematics, and Department of Earth and Environmental Sciences, Columbia University, New York, New York, USA

⁸ Department of Atmospheric Science, Colorado State University, Fort Collins, Colorado, USA

⁹ Division of Earth Environmental System, College of Natural Science, Pusan National University, Busan, Korea

Corresponding author: Dr. Sun-Seon Lee, email: sunseonlee@pusan.ac.kr

24
25
26
27
28
29
30
31
32
33
34
35
36
37
38
39
40
41
42
43
44
45
46

Abstract

Realistic simulations of the Madden-Julian Oscillation (MJO) by global climate models (GCMs) remain a great challenge. To evaluate GCM simulations of the MJO, the U.S. CLIVAR MJO Working Group developed a standardized set of diagnostics, providing a comprehensive assessment of statistical properties of the MJO. Here, we develop a suite of complementary diagnostics that provide discrimination and assessment of MJO simulations based on the perception that the MJO propagation has characteristic dynamic and thermodynamic structures. The new dynamics-oriented diagnostics help to evaluate whether a model produces eastward propagating MJO for the right reasons. The diagnostics include (1) the horizontal structure of boundary layer moisture convergence (BLMC) that moistens the lower troposphere to the east of convection center; (2) the prelude eastward propagation of BLMC that leads the propagation of MJO precipitation by about 5 days; (3) the horizontal structure of 850 hPa zonal wind and its equatorial asymmetry (Kelvin easterly vs. Rossby westerly intensity); (4) the equatorial vertical-longitudinal structure of equivalent potential temperature and convective instability index that reflect the pre-moistening and pre-destabilization processes; (5) the equatorial vertical-longitudinal distribution of diabatic heating that reflects the multi-cloud structure of the MJO; (6) the upper-level divergence that reflects the influence of stratiform cloud heating; and (7) the MJO available potential energy generation that reflects the amplification and propagation of MJO. The models that simulate better three-dimensional dynamic and thermodynamic structures of MJO generally reproduce better eastward propagations. This evaluation identifies a number of shortcomings in representing dynamical and heating processes relevant to the MJO simulation and reveals potential sources of the shortcomings.

47 **Key words: Madden-Julian Oscillation (MJO), GCM simulation of MJO, MJO structure,**
48 **MJO propagation, MJO dynamics, MJO diagnostics**

49

50 **1. Introduction**

51 Tropical atmospheric motion exhibits a significant energy peak on a broad range of 2-10
52 weeks, which is often referred to as tropical intraseasonal variability. The Madden-Julian
53 Oscillation (MJO) is the dominant mode of tropical intraseasonal variability that bridges weather
54 and climate variations (Zhang 2013) and is a major source of global predictability on the sub-
55 seasonal time scale (Waliser et al. 2012). Notable progress has been made in steady improvement
56 of the MJO simulations in global climate models (GCMs), but realistic simulation of the MJO in
57 many current GCMs remains a great challenge (Jiang et al. 2015; Ahn et al. 2017).

58 Statistically, the MJO is defined in the cross-spectrum of wavenumber-frequency domain
59 of outgoing longwave radiation (OLR) and 850 hPa zonal wind (U850) as the spectral
60 components within zonal wavenumbers 1 - 3 and periods of 30-80 days (Wheeler and Kiladis
61 1999; Waliser et al. 2012). To evaluate and track GCMs' simulations of the MJO and identify
62 their major problems, the U.S. Climate Variability and Predictability (CLIVAR) MJO Working
63 Group designed a suite of diagnostics (Waliser et al. 2009). Because of the strong seasonality of
64 the tropical intraseasonal variability, the diagnostics were applied separately to boreal winter
65 from November to April and boreal summer from May to October. The main diagnostic
66 quantities included (a) seasonal variations of the mean circulation (supplementary metric) and
67 intraseasonal variance and (b) properties of the MJO. The properties of the boreal winter MJO
68 characteristics were diagnosed by (1) lag-longitude correlation analysis, (2) single variable
69 empirical orthogonal function (EOF) analysis, (3) single variable frequency-wavenumber spectra,

70 (4) single variable frequency-wavenumber diagram (Wheeler and Kiladis 1999), (5) cross-
71 spectrum in wavenumber-frequency domain (Hendon and Wheeler 2008), (6) multi-variate EOF
72 analysis, and (7) MJO life cycle composites in the horizontal domain (20°S-20°N, 0°-360°E) and
73 in the vertical domain (0°-360°E, 0 hPa-surface). The variables examined primarily included
74 OLR, precipitation, U850, 200 hPa zonal wind (U200), and surface zonal wind except in the life
75 cycle composites where additional variables were used: meridional winds, temperature, humidity,
76 vertical velocity, sea-level pressure (SLP), 200 hPa stream function, as well as sea surface
77 temperature (SST) and surface latent and sensible heat fluxes. These diagnostics provide a
78 comprehensive assessment of the simulated MJO properties, but tend to reflect statistical
79 behavior of the MJO. In addition, for practical applications, one needs to decide which subset of
80 the diagnostics and variables are chosen because some of them are redundant. Furthermore, some
81 diagnostics, for example the structures of the two multi-variate EOF modes, are useful but it is
82 difficult to develop objective measures to quantify the fidelity with which models simulate the
83 structures of EOF modes; the lead-lag correlation between the two leading EOFs reflects
84 propagation, but does not represent simulated propagation skill well (Sperber and Kim 2012).

85 From a dynamical standpoint, the MJO can be defined as a planetary-scale, tropical
86 circulation system, coupled with a multiscale convective complex, moving eastward slowly (~ 5
87 m s^{-1}) over the warm pool of the Indo-Pacific oceans with a rearward tilted baroclinic vertical
88 structure and a coupled Kelvin-Rossby wave (horizontal) structure (Wang and Chen 2017).
89 Based on this perception, the large-scale dynamic and thermodynamic structures of the MJO
90 system should be taken into account in the diagnostics for assessing the fidelity of GCM
91 simulations of the MJO.

92 Observations have shown that anomalous surface low pressure and boundary layer (BL)
93 moisture convergence (BLMC) lead the major convective center (Madden and Julian 1972;
94 Wang 1988a; Hendon and Salby 1994; Salby et al. 1994; Jones and Weare 1996; Maloney and
95 Hartmann 1998; Sperber 2003; Kiladis et al. 2005; Zhang 2005; Tian et al. 2006). To the east of
96 the MJO convective center exist gradual deepening of the moist BL (Johnson et al. 1999;
97 Kemball-Cook and Weare 2001; Tian et al. 2006), increasing convective instability (Hsu and Li
98 2012), poleward winds in the lower free troposphere and associated positive moisture advection
99 (Kim et al. 2014; Wolding and Maloney 2015), and a transition from shallow cumulus, congestus
100 clouds to deep convection and anvil stratiform clouds (Kikuchi and Takayabu 2004; Katsumata
101 et al. 2009; Virts and Wallace 2010; Del Genio et al. 2012; Johnson et al. 2015). These structural
102 features may well be critical to the slow eastward propagation of the MJO.

103 In theory, the MJO structure is a result of the trio-interaction among convective heating,
104 moisture and large-scale (wave and boundary layer) dynamics (Wang et al. 2016). Using a
105 general theoretical model for the MJO, Wang and Chen (2017) have shown that different
106 cumulus parameterization schemes or different parameters in the Betts-Miller scheme (e.g., the
107 convective adjustment time scale) can produce different MJO structural asymmetries, especially
108 the relative intensity of the low-level equatorial Rossby westerlies vs. Kelvin easterlies (the R-K
109 intensity ratio). They have also demonstrated that a large R-K intensity ratio of 2 (similar to the
110 Gill (1980) pattern) corresponds to a non-propagating MJO mode, a ratio of 1.0 (similar to the
111 observed MJO) produces a slow eastward propagation speed of 5 m s^{-1} , while a ratio of 0.6
112 corresponds to a fast propagation of 15 m s^{-1} . This result suggests that a relative strong Kelvin
113 easterly component favors eastward propagation, which is consistent with the previous
114 aquaplanet GCM experiment results of Kang et al. (2014). Using a simplified Bretherton

115 parameterization scheme, Adames and Kim (2016) have suggested a similar relationship between
116 structural asymmetry and propagation speed.

117 To explore why the GCMs have diverse performances in the MJO simulation, Wang and
118 Lee (2017, hereafter WL17) diagnosed 24 GCM simulations and found that the models that
119 simulate better structural asymmetry have better performance in simulation of eastward
120 propagation of the MJO. A variety of structural asymmetry seen from the 24 models studied may
121 arise from different representations of the convective heating. The models' capacity in capturing
122 correct dynamic and thermodynamic structure of the MJO may suggest the models' capability in
123 adequate representation of the convective heating, moisture feedback, wave feedback, convective
124 mixing, low-cloud and stratiform cloud feedback, and BL parameterization, among other
125 processes. To help identify models' deficiencies, it is crucial to assess the performance in
126 simulation of the dynamical and thermodynamic structures and the associated diabatic heating
127 and energy generation processes.

128 Motivated by the aforementioned observations, theoretical findings, and GCM simulation
129 results, in this study, we aim to advance a suite of dynamics-oriented diagnostic metrics for
130 evaluation of GCM simulations of the MJO. Different from the diagnosis of statistical properties,
131 the dynamics-oriented diagnostics are based on the perception that the MJO is a dynamic system
132 with characteristic dynamic and thermodynamic structures that are intimately related to its
133 propagation and instability. The diagnostics will be built based on the observed rudimentary
134 features of the MJO and theoretical understanding of the essential MJO dynamics with specific
135 attention to the processes associated with MJO propagation and amplification/decay. The
136 proposed metrics for each diagnostic variable are intended to be physically intuitive, statistically
137 robust, as well as easy to compute in order to quantitatively measure the GCMs' skill.

138 The dynamics-oriented metrics are different from the existing “process-oriented” metrics
139 of the MJO (e.g., Kim et al. 2014). The latter focus on physical processes related to precipitation
140 (e.g., its interaction with ambient moisture) at grid-point scales and moisture perturbations or
141 normalized gross moist stability (e.g., Benedict et al. 2014), whereas the dynamics-oriented
142 metrics focus on large-scale dynamics and thermodynamic structures of the MJO. The two are
143 complementary to each other. The process-oriented diagnostics intend to explain the failure of a
144 model to produce the observed statistical signals of MJO that can be attributed to deficiencies in
145 model parameterization schemes, especially that for cumulus convection. The diagnostics
146 introduced in the present study help reveal whether a model produces the statistical eastward
147 propagation of the MJO for the right dynamical reason, and identify models’ shortcomings in
148 representing the physical processes relevant to the MJO structure, propagation and amplification,
149 and the potential sources of the shortcomings.

150

151 **2. Data and method**

152 We use Global Precipitation Climatology Project (GPCP) daily precipitation data
153 (Huffman and Bolvin 2013) for the period of 1997-2014 (18 years). For the horizontal and
154 vertical winds, temperature, diabatic heating, and specific humidity, the ERA-Interim reanalysis
155 data with the 1.5° longitude \times 1.5° latitude horizontal resolutions (Dee et al. 2011) are utilized.
156 For all analyses in the present study, intraseasonal (20-70 day) band-pass filtered anomalies
157 during boreal winter (from November to April) are analyzed. The data are interpolated and
158 averaged to $2.5^\circ \times 2.5^\circ$ grids in order to match the model output. Here, we define observations to
159 be GPCP precipitation and ERA-Interim combined.

160 In the present study, we analyze 24 separate 20-year simulations from 22 GCMs (Table 1)
161 that participated in the “Vertical Structure and Diabatic Processes of the MJO: A global model
162 evaluation project”. To characterize, compare, and evaluate the heating, moistening and
163 momentum mixing processes associated with the MJO that are produced by current GCMs, this
164 joint research activity was launched by the WCRP-WWRP/THORPEX MJO task force & YOTC
165 and GASS (<http://www.cgd.ucar.edu/projects/yotc/mjo/vertical.html>) (Petch et al. 2011;
166 Klingaman et al. 2015). Included is a 20-year simulation component which aims at
167 characterization of models’ intrinsic capability to represent the MJO variability and exploration
168 of key processes responsible for high-quality representation of the MJO (Jiang et al. 2015; see
169 also Klingaman et al. 2015 – the synthesis paper). The simulations were integrated for 20 years
170 and provided 6 hourly data with $2.5^\circ \times 2.5^\circ$ horizontal resolution and 22 vertical pressure levels.
171 The detailed descriptions of the project and models can be found in Jiang et al. (2015). We use
172 this dataset and apply the derived metrics to evaluate models’ performance and discuss their
173 potential deficiencies.

174 The diagnostics are developed by regressing 20-70 day filtered anomalies of all variables
175 against the precipitation anomalies at the equatorial eastern Indian Ocean (EIO, 10°S - 10°N , 80° -
176 100°E). This location is chosen because during the boreal winter the Intertropical Convergence
177 Zone (ITCZ) is closest to the equator in the EIO and the mean state tends to be more equatorially
178 symmetric; the corresponding MJO precipitation and circulation are also more symmetric about
179 the equator, and thus are more suitable for the study of the structure of the intrinsic MJO mode
180 with less influence of the mean flow.

181 The MJO mode in reality is affected by the mean climatology. During January through
182 March, the MJO convection after passing through the equatorial EIO tends to move along the

183 Australian monsoon trough and the South Pacific convergence zone and the MJO structure and
184 behavior are more complicated. Similar and even more significant basic state modulation of the
185 MJO mode occurs during boreal summer when the MJO eastward propagation weakens and
186 pronounced northward propagation prevails in monsoon regions; the structure and life cycle are
187 more complex (e.g., Wang and Rui 1990; Wang and Xie 1997; Kemball-Cook and Wang 2001;
188 Jiang et al. 2004; Zhang 2005; Waliser 2006; Kikuchi et al. 2012; Chu et al. 2017; Neena et al.
189 2017). For simplicity and clarity, the present study focuses on the MJO in boreal winter.

190 All dynamics-oriented diagnostics proposed in the present study are measured by the
191 pattern correlation coefficient (PCC) between the observations and model simulations. A
192 conventional method is to directly compute the PCC between the observed and model simulated
193 lag-correlation maps in the Asian–Pacific domain (e.g., Jiang et al. 2015). With that approach,
194 even the models that have no eastward propagation would still have a PCC higher than 0.5. This
195 is because the models may have a local stationary oscillation in the EIO (there are many such
196 cases in observations as well as in the models). In the lag correlation map, the stationary
197 oscillation in the EIO is concentrated in the 85°-95°E and from -20 to +20 days. Unlike Jiang et
198 al. (2015) and WL17, the longitude range between 85°E and 95°E, where the correlation (or
199 regression) coefficients represent local stationary oscillation, is excluded in the calculation of
200 PCC in the time-longitude domain to better depict propagation characteristics. The exclusion of
201 the local stationary oscillation at the reference point makes the poor models' PCCs reduced,
202 while the excellent models' PCC unchanged, so the models' PCC scores spread in a larger range
203 than inclusion of the local oscillation.

204 The generation of MJO available potential energy (APE) is determined by the covariance
205 between diabatic heating (Q) and temperature (T) perturbations (Wang and Li 1994). Before

206 calculation of the regressed field of MJO APE, we computed daily 3-D fields of QT during the
207 20-year period. Then, a 20-70 day band-pass filter was applied ($Q'T'$). The lag zero regression
208 pattern of MJO APE is determined by regression of $Q'T'$ against the 20-70 day band-pass
209 filtered precipitation averaged over the equatorial EIO. The regression amplitudes are scaled to a
210 fixed 3 mm day^{-1} precipitation rate for comparison.

211

212 **3. Performance measures of the simulated MJO**

213 Among several basic features of the MJO, the eastward propagation is its most essential
214 feature (Madden and Julian 1972). It is the slow eastward propagation that characterizes the life
215 cycle of the MJO and produces its prominent 30-60 day timescale. Thus, the eastward
216 propagation is used to represent the primary fidelity of the GCM-simulated MJO compared to the
217 observations.

218 A straightforward way of depicting MJO eastward propagation is the lag-longitude
219 correlation analysis of precipitation anomalies proposed by the MJO Working Group (Waliser et
220 al. 2009). Here we use the 20-70 day filtered GPCP daily precipitation and averaged
221 precipitation within the EIO ($10^{\circ}\text{S}-10^{\circ}\text{N}$, $80^{\circ}-100^{\circ}\text{E}$) as a reference region to construct lag-
222 longitude correlation diagrams. The reference region covers a relatively large area (20×20
223 degrees) to emphasize the planetary scale of the MJO.

224 Figure 1a shows the observed lag-longitude correlation map. The observed MJO
225 precipitation exhibits continuous eastward propagation from 50°E to 180°E with an average
226 speed of about 5 m s^{-1} . Simulation performance can readily be measured by the PCC between the
227 observed and simulated propagation diagrams on the time-longitude domain ($50^{\circ}-180^{\circ}\text{E}$, from
228 day -20 to day 20) by exclusion of the longitude range between 85°E and 95°E for the reason

229 discussed in Section 2. Figure 1d shows the PCC skill of each model, which varies from 0.20 to
230 0.96. Based on the PCC values, we select the 6 best models, with an average PCC of 0.93
231 (hereafter excellent models), and the 6 poorest models with an average PCC of 0.47 (hereafter
232 poor models). Figures 1b and 1c present the composite lag-longitude correlation diagrams for the
233 excellent and poor models, respectively. Obviously, the excellent models simulate realistic
234 eastward propagation, while the poor models fail in a statistical sense. In general, higher PCC
235 values correspond to more systematic eastward propagation of both the wet and dry anomalies
236 and better propagation speeds over the equatorial Indo-Pacific warm pool regions.

237 Note that the PCC value is an overall assessment of the propagation feature; but it cannot
238 distinguish between quality in simulated propagation speed and quality in propagation distance
239 and continuity. Statistically, the eastward propagation can also be reflected in the single variable
240 frequency-wavenumber diagram or cross-spectrum in wavenumber-frequency domain as
241 proposed by the MJO Working Group, where the ratio of the spectral power for the eastward and
242 westward propagating components (the E/W ratio) on the MJO time and spatial scales was used
243 to measure the eastward propagation skill (Kim et al. 2009). This spectral measure (the E/W ratio)
244 has been shown to correlate very well with the PCC skill score in the lag-longitude diagram
245 (CC=0.78 for 27 GCM simulations) (Jiang et al. 2015). Therefore, use of the lag-longitude
246 correlation diagram is probably a simple, yet sufficient, way to measure the MJO propagation
247 and performance skill.

248 It is worth noting that the poor models that do not produce the statistical eastward
249 propagating signals of the MJO may still produce infrequent individual MJO events (Ling et al.
250 2017). Any diagnostics based on statistical approaches (e.g., regression, composite) would not be
251 able to characterize signals of these infrequently produced MJO events. This is a common

252 limitation of all diagnostics that seek statistical composite signals of the MJO. In future study,
253 we plan to apply the dynamical diagnostics to be introduced in section 4 to individual MJO
254 events simulated by GCMs regardless of whether they can produce statistical eastward
255 propagating signals of the MJO.

256

257 **4. Diagnostic metrics**

258 **a. Structure and propagation of boundary layer moisture convergence**

259 Madden and Julian (1972) noted an important feature of the MJO, i.e., the low SLP
260 anomaly locates to the east of the major convective center. This feature has been discussed little
261 in the MJO literature, although the BL convergence in the anomalous low was emphasized
262 (Wang 1988b; Hendon and Salby 1994; Maloney and Hartmann 1998). The anomalous low
263 implies not only BL convergence but also the strength of the Kelvin wave easterly and associated
264 anomalous Walker cell to the east of the MJO convection, which may play a critical role in the
265 MJO propagation. In the trio-interaction theoretical model, Wang et al. (2016) has used three
266 different simplified cumulus parameterization schemes to represent the moisture feedback. In
267 that model, no matter which convective parameterization scheme is used, without the BL effect,
268 an initial Gill-like disturbance will be decoupled with the Kelvin waves moving eastward and the
269 Rossby waves westward. It is the BLMC that couples the Kelvin and Rossby waves and
270 convection together, and selects eastward propagation under different heating schemes. WL17
271 showed that the BLMC favors the MJO eastward propagation by generating lower-tropospheric
272 heating and APE to the east of precipitation center. Given the observed feature and the insight
273 gained from theoretical work, we recommend the BLMC be considered as one of the diagnostic
274 targets.

275 Figure 2a shows the observed horizontal structure of the BLMC. A notable feature is the
276 zonal asymmetry of the BLMC with regard to the MJO precipitation anomaly. The observed
277 BLMC extends about 60° longitudes east of the EIO (90°E) with a center located at 130°E. The
278 zonal asymmetry in the BLMC can be better seen from the equatorial distribution of BLMC
279 averaged between 5°S and 5°N (Fig. 2b). The observation and excellent model composite show
280 strong BLMC over the Maritime Continent and equatorial western Pacific between 120°-160°E
281 while the poor model composite shows little BLMC over the corresponding region. Figure 2c
282 shows that the quality of simulated MJO eastward propagation is significantly linked to the
283 simulated BLMC structure with a positive CC of 0.79.

284 In addition to the BLMC structure, the observed BLMC propagates eastward
285 systematically from 50°E to 180°E at a speed of about 5 m s⁻¹ (Fig. 3a). More importantly, the
286 propagation of the BLMC leads that of precipitation by about 5 days. Since the BLMC leads the
287 precipitation propagation, the BLMC should be considered as an indicator of the MJO eastward
288 propagation. The performance of GCMs in simulating BLMC propagation can be measured by
289 the PCC score between the observation and simulations in the domain of (-20 – +20 day and
290 50°–180°E). Figure 3b shows a strong positive correlation (CC=0.83) between the performance
291 of MJO propagation performance and that of the BLMC propagation, indicating that the models
292 simulating better BLMC propagation reproduce more realistic eastward propagation of the MJO.

293 **b. Zonal asymmetry in the low-level circulation**

294 It has been found that the observed MJO propagation is intrinsically linked to its low-
295 level horizontal circulation structure (WL17). The observed 850 hPa circulation anomaly has a
296 Kelvin wave component to the east of heating and a symmetric Rossby wave component to the
297 west of the heating (Fig. 4a). As pointed out by WL17, the observed MJO structure, while

298 resembling a Gill (1980) pattern, has notable differences with the Gill pattern in the relative
299 strength and zonal extent of the Kelvin and Rossby (K-R) wave components. The zonal extent
300 ratio of the Kelvin easterly vs. that of the Rossby westerly is 3.0 in the Gill pattern but only 2.1
301 in the observed MJO; the maximum Rossby westerly speed vs. the maximum Kelvin easterly
302 speed is 2.2 in the Gill pattern but only 0.8 in the observed MJO. The different structures likely
303 arise from the nature of the heating: the heating is specified in the Gill model whereas is
304 interactive with the circulation of the MJO, although other factors, such as basic flows and
305 uneven boundary conditions, may also affect the structure. The GCMs may produce different
306 horizontal structures because their cumulus parameterization schemes may lead to different
307 interactions between convective heating and equatorial wave dynamics. Thus, the horizontal
308 structure of the MJO should be an indispensable target of the diagnostics.

309 To quantify the performance in reproducing the observed U850 structure (Fig. 4a), we
310 measure the overall shape of U850 in the domain of (15°S-15°N, 50°-160°E) using the PCC
311 between the observed and simulated U850. Figure 4c shows a robust relationship between the
312 simulated MJO eastward propagation and the U850 structure with a $CC=0.74$ ($p<0.01$).

313 The difference between the excellent and poor simulations lies mainly in the zonal
314 asymmetries in the relative intensity and zonal extent of the equatorial Kelvin (wave) easterlies
315 vs. Rossby (wave) westerlies (Fig. 4b). The equatorial structure of U850 in the observation is
316 reproduced well by the excellent models but not by the poor models (Fig. 4b). An alternative
317 metric for depicting the U850 structural asymmetry is the ratio of maximum intensity between
318 the equatorial Kelvin wave easterlies and the equatorial Rossby wave westerlies. Figure 4d
319 shows that the U850 asymmetric index simulated in the various models is well correlated with
320 the performance of the simulated MJO eastward propagation ($CC=0.67$, $p<0.01$), but the

321 relationship seems to be nonlinear, so the linear CC is not as high as the two-dimensional U850
322 structure. The observed ratio of maximum Kelvin easterly vs. Rossby westerly is 1.25, indicating
323 stronger Kelvin easterly waves than Rossby westerly waves. The excellent models' mean is 1.16,
324 resembling the observed MJO structure, but the poor models' mean is 0.50, which resembles the
325 Gill pattern.

326 **c. Vertical structure of the equivalent potential temperature and convective instability**

327 In the observations, deepening of the lower-tropospheric moist layer occurs before the
328 enhanced deep convective phase of the MJO (e.g., Blade and Hartmann 1993; Johnson et al.
329 1999; Kemball-Cook and Weare 2001; Tian et al. 2006; Zhu et al. 2009). This is also
330 demonstrated by the eastward shift of the maximum BL specific humidity with respect to the
331 convective center and a rearward (westward) tilted moisture field in the lower troposphere
332 (Sperber 2003; Tian et al. 2006). Hsu and Li (2012) have shown that the equivalent potential
333 temperature (EPT) also exhibits the rearward tilted structure in the lower troposphere, and the
334 convective instability measured by the difference in the EPT between the BL and middle
335 troposphere is enhanced before the arrival of major MJO convection. The vertical gradient of
336 EPT can indicate convective instability only if the layer is lifted to become saturated. Jiang et al.
337 (2015) examined the vertical structure of the specific humidity and found the simulated vertical
338 structure is very well correlated with the simulated eastward propagation. Building on all these
339 previous work, the vertical EPT profile representing the moist thermodynamic structure of the
340 MJO is considered as a basic diagnostic for the MJO.

341 The observed moist thermodynamic feature is confirmed by the vertical profile of the
342 EPT over the EIO (Fig. 5a). The maximum EPT is found at 500 hPa, overlaying the convective
343 center. There is a salient rearward (westward and upward) tilt of the EPT in the lower

344 troposphere below the 500 hPa level, reflecting the gradual deepening of the moist layer toward
345 the west on the east side of the convective center. Also of interest is the forward (eastward) tilt of
346 the EPT in the upper troposphere between 400 and 200 hPa. The forward tilt, while not discussed
347 much in the literature, may be mainly attributed to the positive temperature anomaly to the east
348 of the deep convection center (Fig. 10b in WL17) because in the upper troposphere the moisture
349 contribution to the EPT generation is small. This feature is important for the MJO eddy APE
350 generation as will be discussed shortly. However, it remains unclear what causes the upper-level
351 positive temperature anomaly to the east of MJO deep convective region. Net radiative heating
352 may be a candidate factor (Del Genio and Chen 2015; Johnson et al. 2015). Whether this is
353 related to the vertically propagating Kelvin waves (Virts et al. 2010) or the baroclinic Kelvin
354 wave signature to the east of the MJO heating needs to be further investigated.

355 The rearward tilt of the EPT in the lower troposphere in Fig. 5a suggests that the pre-
356 moistening and pre-destabilization processes precede the MJO convective peaks. Following Hsu
357 and Li (2012) and WL17, a convective instability index is defined by the 850 hPa EPT minus
358 400 hPa EPT averaged between 120° and 150°E, which measures the pre-destabilizing conditions
359 to the east of the MJO convection. Selection of the longitudinal range is based on the zonal
360 distributions of the convective instability parameter in the observation, excellent model
361 composite, and poor model composite (Fig. 5b). The distinct zonal asymmetry is simulated well
362 by the excellent models, but the poor models cannot capture the observed high convective
363 instability between 120° and 150°E.

364 To quantify the characteristic EPT profile, we use the PCC between the observed and
365 model simulated vertical profiles of the EPT along the equator from 40°E to 180°E and from
366 1000 hPa to 200 hPa. As shown in Fig. 5c, the PCC score of the simulated vertical structure of

367 EPT is positively correlated with the MJO propagation score ($CC=0.77$, $p<0.01$). Another metric
368 measuring the pre-destabilization, i.e. the convective instability index, is also reasonably well
369 correlated to the simulated MJO propagation skills in all 24 GCM simulations with a positive CC
370 of 0.62.

371 **d. Zonally asymmetric distribution of diabatic heating**

372 Observations have shown a continuous (or stepwise) transition from the shallow cumulus
373 and congestus clouds to deep convective clouds and stratiform clouds (Kikuchi and Takayabu
374 2004; Katsumata et al. 2009; Virts and Wallace 2010; Del Genio et al. 2012; Johnson et al. 2015).
375 Associated with the transition of clouds, the diabatic heating of the MJO possesses a vertical
376 rearward tilted structure (Sperber 2003; Jiang et al. 2011). The lower tropospheric heating has
377 been speculated to be important to the MJO (Li et al. 2009; Zhang and Song 2009). The
378 importance of the stratiform cloud heating and its interaction with the second baroclinic mode
379 and moisture has also been found to support MJO growth and propagation (Mapes 2000; Kuang
380 2008; Fu and Wang 2009).

381 Diabatic heating is dominated by condensational heating in the tropics and thus is an
382 indicator of the precipitating cloud distributions. The longitudinal distribution of diabatic heating
383 along the equator may suggest how the GCMs capture the observed transition from shallow
384 cumuli, congestus to deep convective and stratiform clouds. The GCM simulated cloud
385 distribution provides critical information about cumulus parameterization and representation of
386 cloud in the GCMs.

387 Figure 6a shows anomalous diabatic heating distribution and anomalous Walker cell in
388 the zonal-vertical equatorial plane. The heating was computed from the reanalysis data using the
389 budget residual analysis of Yanai et al. (1973). The diabatic heating results here are in good

390 agreement with those of Johnson et al. (2015) which were calculated using sounding data during
391 the DYNAMO field experiments (Yoneyama et al. 2013). The observed lower tropospheric
392 heating is clearly leading the mid-tropospheric deep convective heating (Fig. 6a), suggesting the
393 existence of shallow and congestus clouds; meanwhile, the upper tropospheric heating between
394 500 and 300 hPa tends to expand westward from the deep convective center to 60°E, suggesting
395 that stratiform clouds may trail deep convection. Associated with the diabatic heating field are
396 two Walker-like east-west cells (Madden and Julian 1972). One is to the west and the other to the
397 east of the major convection. We refer the one located to the east as the “front Walker cell
398 (FWC)” as it leads the MJO propagation. The ascending branch of the FWC is coupled with the
399 deep IO convection; whereas the descending branch corresponds to reduced diabatic heating over
400 the western Pacific. The FWC can be enhanced by the zonal heating gradients between the IO
401 and western Pacific (Chen and Wang 2017). The excellent models simulate realistic vertical tilt
402 of diabatic heating and FWC (Fig. 6b) while the poor models fail to reproduce them (Fig. 6c), as
403 previously noted in Jiang et al. (2015) and WL17. In the poor models, the diabatic heating is
404 narrowly trapped in the deep convective regions with a center slightly to the west of precipitation
405 center, showing little sign of the lower tropospheric heating leading deep convection and the
406 westward extension of the upper tropospheric heating.

407 For a given MJO precipitation rate of 3 mm day^{-1} , both excellent and poor GCMs tend to
408 produce stronger low-level wind responses than the observations, especially the low-level
409 equatorial westerly anomalies. The strong responses of the low-level circulations in the models
410 seem to be related to the lower maximum heating and larger vertical heating gradients in the
411 lower troposphere. The maximum heating center is located around 420 hPa in reanalysis, while it
412 is around 460 hPa in the excellent models and 500 hPa in the poor models. In addition, the

413 vertical heating gradients below 600 hPa simulated in the excellent models are twice large as
414 those in reanalysis; even in the poor models this vertical gradient is larger than the observed.

415 The model performance in capturing the vertical heating structure is measured by the
416 PCC between the observed and simulated vertical distributions of the equatorial diabatic heating
417 in the domain of (40°-180°E, 1000-200 hPa). As shown in Fig. 6d, the PCC score between the
418 observed and simulated vertical profile of equatorial diabatic heating is highly indicative of the
419 quality of model simulated propagation (CC=0.86, $p<0.01$). Thus, the quality of GCM's
420 simulation of diabatic heating processes is an important metric for the evaluation of MJO
421 simulation.

422 **e. Zonal asymmetry in the upper-level divergence and diabatic heating**

423 The upper-level divergence is a good indicator of the MJO eastward propagation
424 (Adames and Wallace 2014). It also reflects the upper-level precipitation heating (deep
425 convection and the stratiform clouds tailing it). The longitudinal distribution of the 200 hPa wind
426 divergence along the equator may reveal how the GCMs capture the observed transition from
427 deep convective to stratiform clouds and how the GCMs produce upper-level divergence sources
428 which are important for the tropical-extratropical teleconnection.

429 Figure 7a shows the observed 200 hPa winds and associated divergence when the
430 convective center is located at the EIO. The upper-level circulation is approximately out of phase
431 with that at 850 hPa (Fig. 4a), consisting of a pair of anticyclonic Rossby gyres and associated
432 equatorial easterlies to the west of the convection and a Kelvin wave high and associated
433 equatorial westerlies to the east of the convective center. Note that the equatorial U200 exhibits a
434 strong zonal asymmetry with the Rossby easterly anomalies being much stronger than the Kelvin
435 westerly anomalies, which is opposite to the zonal asymmetry in the U850. The 200 hPa

436 divergence center is located to the west of the convection center and extends westward to the
437 western IO, which largely coincides with the 300 hPa diabatic heating. Thus, we speculate that
438 the westward extension of the 200 hPa divergence is primarily attributed to the westward
439 extension of the 300 hPa diabatic heating produced by the stratiform clouds. There is also 200
440 hPa convergence occurring over the South China Sea and Philippines and the equatorial western
441 Pacific between 150°E and 180°E. Associated with the convergence over the Philippines is the
442 divergence over East Asia and subtropical western Pacific, a sign of teleconnection with
443 midlatitude. The aforementioned observed features are well simulated by the excellent models
444 (Fig. 7b). But in the poor model, the divergence does not extend westward to the western IO and
445 very weak convergence occurs to the east of the major convective center (Fig. 7c).

446 Similar to the low-level circulation field, we calculate the PCC of 200 hPa divergence
447 between the observation and simulations (15°S-15°N, 50°-160°E) to quantify the models'
448 capability for capturing the upper-level circulation. Figure 7d shows that the models simulating
449 better upper-level divergence have better simulation of the MJO eastward propagation with a CC
450 of 0.75, suggesting that the 200 hPa divergence field is a useful metric for gauging the GCMs'
451 performance. Similarly, we measure the PCC of 300 hPa diabatic heating over the same region
452 (15°S-15°N, 50°-160°E). As shown in Fig. 7e, the models' PCC skill in simulation of the 300 hPa
453 diabatic heating is well correlated with the models' performance in simulation of the MJO
454 propagation (CC=0.74). Thus, the 200 hPa divergence (or 300 hPa diabatic heating) can be used
455 for evaluation of GCMs' simulation of the upper-level circulation.

456 **f. MJO available potential energy generation**

457 The observed MJO convective anomalies show amplification over the warm IO and
458 equatorial western Pacific, decaying over the Maritime Continent and near the dateline when

459 approaching the cold tongue of the eastern Pacific (Madden and Julian 1972; Wang and Rui
460 1990). The SST largely controls the basic state moist static energy (MSE) distribution, thus the
461 MSE advection associated with MJO. The SST also regulates the intensity of deep convection,
462 thereby affecting the amplitude of the MJO. Over the EIO the amplification and propagation of
463 the MJO can be diagnosed by energetic analysis. The eddy APE is the energy source for MJO
464 development. WL17 showed that the large difference in eddy APE generation between the
465 excellent and poor models lies in its zonal asymmetry. Thus, we consider the vertical structures
466 of eddy APE generation as an indicator for the MJO simulation.

467 Figure 8a displays the rate of generation of the MJO APE along the equator from 40°E to
468 180°E. The eddy APE is determined by the phase overlapping (covariance) of the diabatic
469 heating and temperature anomalies (heating where air is anomalous warm and cooling where
470 anomalous cold). Near the major convective center, the observed APE generation rate is large in
471 the upper-troposphere (above 550 hPa) because the diabatic heating reaches a maximum (Fig. 6a)
472 and the air tends to be warmer than normal (Fig. 8a). Notably, the observed APE generation to
473 the east of 90°E is significantly larger than that to the west of 90°E, especially in the lower
474 troposphere. The zonal asymmetry in APE generation with respect to the MJO precipitation
475 center is primarily due to (a) positive temperature anomalies occurring to the east of the major
476 convection region (Fig. 8a) and (b) the lower tropospheric heating occurring to the east of the
477 90°E (Fig. 6a).

478 Note that the MJO APE generated in the major convective region mainly contributes to
479 the amplification of the MJO. But more generation of APE to the east of the major convective
480 center facilitates the eastward propagation of the MJO because the APE would be converted to
481 the MJO kinetic energy during which the upward motion is promoted to the east of the MJO

482 convection.

483 The PCC between the observed and simulated APE generation rate over the equatorial
484 domain (40°E-180°E and 1000 hPa-200 hPa) is used to measure this simulated asymmetry. The
485 performance of the models in simulation of the APE generation has a significant positive
486 correlation (CC=0.84) with that of model-simulated MJO propagation (Fig. 8b).

487

488 **5. Summary**

489 Despite considerable progress made in the last two decades, simulations of the MJO in
490 GCMs still suffer from notable shortcomings. The CLIVAR MJO Working Group developed a
491 standardized, comprehensive set of diagnostics for assessing models' successes and
492 shortcomings in the MJO simulations. These diagnostics tend to reflect statistical behaviors of
493 the MJO. The MJO is a dynamic system with characteristic dynamic and thermodynamic
494 structures that are intimately related to its propagation and instability. Within this conceptual
495 framework, an additional and complementary set of dynamics-oriented diagnostics is presented
496 in this current study. This set of diagnostics aims to focus on the observed fundamental
497 dynamical structures and thermodynamic features of the MJO deemed important to its
498 propagation and amplification/decay. In order to quantitatively assess the GCMs' skill at the
499 MJO propagation and reasons for possible shortcomings, the metrics for various diagnostic fields
500 are designed, aiming to be physically intuitive, statistically robust, and easy to compute.

501 In the present study, the MJO propagation is depicted by the lag-correlated precipitation
502 anomalies along the equatorial channel with reference to the EIO convective center (Fig. 1). It is
503 also desirable to assess a similar lag correlation map with reference to the Maritime Continent
504 and western Pacific convection (WL17). To capture and quantify the fidelity of a GCM to

505 replicate the observed elementary features of the MJO during boreal winter (NDJFMA), the
506 dynamics-oriented diagnostics include the 7 components summarized in Table 2. (1) The
507 horizontal structure of BLMC (Fig. 2) that moistens the lower troposphere to the east of
508 convection center. (2) The prelude propagation of the BLMC (Fig. 3), which leads
509 precipitation propagation by about 5 days. (3) The horizontal structure and zonal asymmetry in
510 U850 (Fig. 4), which is characterized by the relative intensity of the Kelvin vs. Rossby wave
511 components that is intrinsically linked to the MJO propagation. This low-level horizontal
512 circulation quality may be relevant to explanation of the importance of the horizontal advective
513 moistening for eastward propagation (Maloney 2009). (4) The equatorial vertical structure of the
514 EPT (Fig. 5) or MSE, which reflects the observed pre-moistening process that gradually deepens
515 the lower tropospheric moist layer and increases convective instability. (5) The equatorial
516 vertical-longitudinal distribution of diabatic heating and associated anomalous Walker cells (Fig.
517 6), which reflects well the multi-cloud structure of the MJO convective complex and a
518 continuous transition from shallow cumulus-congestus clouds to deep convective-stratiform
519 clouds. (6) The upper-level divergence and diabatic heating (Fig. 7) which is zonally asymmetric
520 and a good indicator of the MJO deep convective and stratiform clouds. Its longitudinal
521 distribution may reveal how the GCMs simulate the eastward propagation and the sources for
522 teleconnection to mid-latitude. (7) The generation of MJO APE (Fig. 8), which reflects the
523 amplification and propagation of the MJO, in particular the amplification over the IO and
524 equatorial western Pacific warm pool and the decay over the Maritime Continent (Zhang and
525 Ling 2017) and the central Pacific. The quality of the model simulated 7 diagnostic fields reflect
526 very well the quality of the model simulated eastward propagation of the MJO with the PCCs
527 ranging from 0.74 to 0.86.

528 To facilitate a quick assessment of individual model's performance on simulation of the 7
529 diagnostic fields, we have calculated the averaged PCC skill scores for each group of diagnosed
530 models (excellent, good, fair, and poor) as a reference for comparison. The results are shown in
531 Table 3. By comparison of the performance from any individual model with the reference skills
532 shown in Table 3, one can get a general idea about how good is the individual model's
533 simulation quality compared to the 24 model simulations.

534 Some of these metrics shown in Table 2 are well correlated with other metrics. For
535 example, the correlation between the BLMC propagation skill and U850 structure skill is 0.67.
536 But, we keep all of the metrics listed in Table 2 mainly based on the consideration of intrinsic
537 dynamics. As discussed earlier, each diagnostic field is selected to represent a specific dynamical
538 feature or process. This does not mean that all the diagnostic fields are equally important. Use of
539 relatively independent diagnostic fields may lead to a more concise set of the diagnostics. For
540 instance, if the diabatic heating, propagation of the BLMC and the structure of the U850 are
541 chosen as the metrics, their weighted combination (derived by multi-regression),

542 $0.49 \times \text{Heating structure} + 0.42 \times \text{BLMC propagation} + 0.14 \times \text{U850 structure}$
543 can yield a PCC skill score of 0.94 for representing the MJO precipitation propagation.

544 These diagnostics help to identify the shortcomings of the GCMs in representing not only
545 the dynamic structure and thermodynamic features but also the physical processes relevant to the
546 MJO propagation and the potential sources of the shortcomings. For instance, a lack of pre-
547 moistening and pre-destabilization as well as the prelude BLMC propagation may hint
548 problems in representing the BL convergence and its interaction with shallow-congestus clouds
549 through lower-tropospheric convective mixing and low-cloud feedback. Deficiencies in the
550 simulated thermodynamic structure, diabatic heating distribution and upper-level divergence may

551 be indicative of problems in models' representation of the formation of congestus clouds and
552 stratiform clouds. A deficient horizontal structure may be related to the cumulus
553 parameterization or uncertain parameters within parameterization schemes (e.g. Kim and Seo
554 2017). On the other hand, a deficient horizontal circulation could result in erroneous horizontal
555 moisture advection. The latter has been shown to be important for MJO propagation (Maloney
556 2009; Maloney et al. 2010; Sobel and Maloney 2012, 2013; Adames and Kim 2016; Jiang 2017).

557 By illustrating the dynamical structures associated with simulated MJO disturbances, the
558 diagnostics introduced here help us to evaluate whether models produce the MJO (according to
559 the basic statistical diagnostics) for the right reasons (according to the basic dynamic
560 diagnostics). That said, the diagnostics were not designed to confirm or refute specific theories
561 for the underlying macroscopic mechanisms for the very existence of the MJO and its properties
562 that are repeatedly observed. For example, a number of studies argue for the role of radiative
563 feedbacks in driving the MJO (e.g., Raymond 2001; Bony and Emanuel 2005; Andersen and
564 Kuang 2012; Sobel and Maloney 2012, 2013; Arnold and Randall 2015; Adames and Kim 2016).
565 The diagnostics introduced here do not include this possible aspect of the MJO. Also, this set of
566 dynamics-oriented diagnostics is not exclusive of other factors that may impact the MJO
567 simulations. For instance, correct simulation of seasonal-mean moisture is important for the MJO
568 simulation (Kim et al. 2011; Benedict et al. 2014; Gonzalez and Jiang 2017; Jiang 2017), correct
569 simulation of the annual cycle of the mean state and the seasonal migration of the convective
570 variance is also important. The boreal summer intraseasonal oscillation is more complex due to
571 its more complicated interaction with the mean state, including stronger land-ocean-atmosphere
572 interactions. Addressing the boreal summer version of the MJO to the same level as addressed
573 here will likely require additional/different diagnostics. The MJO interaction with the underlying

574 ocean, interaction with the extratropics, and other factors are not included in this study.
575 Diagnostics to assess these additional factors deserve to be developed.

576

577 **Acknowledgments**

578 This work is supported by the National Science Foundation of (Climate Dynamics
579 Division Award No. AGS-1540783) and the NOAA/CVP #NA15OAR4310177, as well as the
580 Global Research Laboratory (GRL) Program of the Korean Ministry of Education, Science and
581 Technology (MEST, #2011-0021927). This is publication No. XXXX of the SOEST, publication
582 No. YYYY of IPRC, and publication No. ZZZ of the Earth System Modeling Center (ESMC).
583 PMEL contribution number 4664. EDM was supported by the National Science Foundation
584 under grant AGS-1441916, and the National Oceanic and Atmospheric Administration under
585 grants NA15OAR4310098 and NA15OAR4310099.

586

587 **References**

- 588 Adames, Á. F., and D. Kim, 2016: The MJO as a dispersive, convectively coupled moisture
589 wave: Theory and observations. *J. Atmos. Sci.*, 73, 913-941.
- 590 Adames, Á. F., and J. M. Wallace, 2014: Three-dimensional structure and evolution of the
591 vertical velocity and divergence fields in the MJO. *J. Atmos. Sci.*, 71, 4661–4681.
- 592 Ahn, M. S., D. Kim, K. Sperber, E. Maloney, D. Waliser, H. Hendon, and on behalf of WGNE
593 MJO Task Force, 2017: MJO simulation in CMIP5 climate models: MJO skill metrics
594 and process-oriented diagnosis. *Clim. Dyn.*, In press.
- 595 Andersen, J. A., and Z. Kuang, 2012: Moist static energy budget of MJO-like disturbances in the
596 atmosphere of a zonally symmetric aquaplanet. *J. Climate*, 25, 2782-2804.

597 Arnold, N. P., and D. A. Randall, 2015: Global-scale convective aggregation: Implications for
598 the Madden-Julian Oscillation. *J. Adv. Model. Earth Syst.*, **7**, 1499–1518.

599 Bao, Q., and Coauthors, 2013: The flexible global ocean-atmosphere-land system model, spectral
600 version 2: FGOALS-s2. *Adv. Atmos. Sci.*, **30**, 561–576.

601 Batté, L. and F. J. Doblas-Reyes, 2015: Stochastic atmospheric perturbations in the ECEarth3
602 global coupled model: impact of SPPT on seasonal forecast quality. *Clim. Dyn.* **45**, 3419–
603 3439.

604 Benedict, J. J., E. D. Maloney, A. H. Sobel, and D. M. Frierson, 2014: Gross moist stability and
605 MJO simulation skill in three full physics GCMs. *J. Atmos. Sci.*, **71**, 3327–3349.

606 Blade, I., and D. L. Hartmann, 1993: Tropical intraseasonal oscillations in a simple nonlinear
607 model. *J. Atmos. Sci.*, **50**, 2922–2939.

608 Bony, S., and K. A. Emanuel, 2005: On the role of moist processes in tropical intraseasonal
609 variability: Cloud–radiation and moisture–convection feedbacks. *J. Atmos. Sci.*, **62**,
610 2770-2789.

611 Chen, G. and B. Wang, 2017: Effects of enhanced front Walker cell on the eastward propagation
612 of MJO. *J. Climate*, Submitted.

613 Chu, J.-E., B. Wang, J.-Y. Lee, and K.-J. Ha, 2017: Boreal summer intraseasonal phases
614 identified by nonlinear multivariate empirical orthogonal function-based self-organizing
615 map (ESOM) analysis. *J. Climate*, **30**, 3513-3528.

616 Côté, J., S. Gravel, A. Méthot, A. Patoine, M. Roch, and A. Staniforth, 1998: The operational
617 CMC-MRB Global Environmental Multiscale (GEM) model. Part I: Design
618 considerations and formulation. *Mon. Wea. Rev.*, **126**, 1373–1395.

619 Dee, D. P., and Coauthors, 2011: The ERA-Interim reanalysis: configuration and performance of

620 the data assimilation system. *Quart. J. Roy. Meteor. Soc.*, 137, 553–597.

621 Del Genio, A. D., and Y. Chen, 2015: Cloud-radiative driving of the Madden-Julian oscillation
622 as seen by the A-Train. *J. Geophys. Res.*, 120, 5344–5356.

623 Del Genio, A. D., Y. Chen, D. Kim, and M.-S. Yao, 2012: The MJO transition from shallow to
624 deep convection in CloudSat/CALIPSO data and GISS GCM simulations. *J. Climate*, 25,
625 3755–3770.

626 Fu, X., and B. Wang, 2009: Critical roles of the stratiform rainfall in sustaining the Madden–
627 Julian oscillation: GCM experiments. *J. Climate*, 22, 3939–3959.

628 Gill, A. E., 1980: Some simple solutions for heat-induced tropical circulation. *Q. J. R. Meteorol.*
629 *Soc.*, 106, 447–462.

630 Gonzalez, A. O., and X. Jiang, 2017: Winter mean lower tropospheric moisture over the
631 Maritime Continent as a climate model diagnostic metric for the propagation of the
632 Madden-Julian oscillation. *Geophys. Res. Lett.*, 44, 2588–2596.

633 Hendon, H. H., and M. C. Wheeler, 2008: Some space–time spectral analyses of tropical
634 convection and planetary-scale waves. *J. Atmos. Sci.*, 65, 2936–2948.

635 Hendon, H. H., and M. L. Salby, 1994: The life cycle of the Madden–Julian oscillation. *J. Atmos.*
636 *Sci.*, 51, 2225–2237.

637 Hogan, T. F., and Coauthors, 2014: The Navy Global Environmental Model, *Oceanography*, 27,
638 64–74.

639 Hsu, P.-C., and T. Li, 2012: Role of the boundary layer moisture asymmetry in causing the
640 eastward propagation of the Madden-Julian Oscillation. *J. Climate*, 25, 4914–4931.

641 Huffman, G. J., and D. T. Bolvin, 2013: Version 1.2 GPCP one-degree daily precipitation data
642 set documentation. [Available at <ftp://precip.gsfc.nasa.gov/pub/1dd->

643 [v1.2/1DD_v1.2_doc.pdf.](#)]

644 Jiang, X., 2017: Key processes for the eastward propagation of the Madden-Julian Oscillation
645 based on multimodel simulations. *J. Geophys. Res. Atmos.*, 122, 755–770.

646 Jiang, X., D. E. Waliser, P. K. Xavier, J. Petch, N. P. Klingaman, S. J. Woolnough, B. Guan, G.
647 Bellon, T. Crueger, and C. DeMott, 2015: Vertical structure and physical processes of the
648 Madden-Julian oscillation: Exploring key model physics in climate simulations. *J.*
649 *Geophys. Res. Atmos.*, 120, 4718–4748.

650 Jiang, X., T. Li, and B. Wang, 2004: Structures and mechanisms of the northward propagating
651 boreal summer intraseasonal oscillation. *J. Climate*, 17, 1022-1039.

652 Johnson, R. H., J. H. Ruppert Jr., and M. Katsumata, 2015: Sounding-based thermodynamic
653 budgets for DYNAMO. *J. Atmos. Sci.*, 72, 598–622.

654 Johnson, R. H., T. M. Rickenbach, S. A. Rutledge, P. E. Ciesielski, and W. H. Schubert, 1999:
655 Trimodal characteristics of tropical convection. *J. Climate*, 12, 2397-2418.

656 Jones, C., and B. C. Weare, 1996: The role of low-level moisture convergence and ocean latent
657 heat flux in the Madden-Julian Oscillation: An observational analysis using ISCCP data
658 and ECMWF analyses. *J. Climate*, 9, 3086-3104.

659 Kang, I. S., F. Liu, M. S. Ahn, Y. M. Yang, and B. Wang, 2014: Role of SST structure on
660 convectively coupled Kelvin-Rossby waves and its implication on MJO formation. *J.*
661 *Climate*, 26, 5915-5930.

662 Katsumata, M., R. H. Johnson, and P. E. Ciesielski, 2009: Observed synoptic-scale variability
663 during the developing phase of an ISO over the Indian Ocean during MISO. *J. Atmos.*
664 *Sci.*, 66, 3434–3448.

665 Kemball-Cook, S., and B. C. Weare, 2001: The onset of convection in the Madden-Julian

666 oscillation. *J. Climate*, 14, 780–793.

667 Kemball-Cook, S., and B. Wang, 2001: Equatorial waves and air-sea interaction in the boreal
668 summer intraseasonal oscillation. *J. Climate*, 14, 2923–2942.

669 Kikuchi, K., and Y. N. Takayabu, 2004: The development of organized convection associated
670 with the MJO during TOGA COARE IOP: Trimodal characteristics. *Geophys. Res. Lett.*,
671 31, L10101.

672 Kikuchi, K., B. Wang, and Y. Kajikawa, 2012: Bimodal representation of the tropical
673 intraseasonal oscillation. *Clim. Dyn.*, 38, 1989–2000.

674 Kiladis, G. N., K. H. Straub, and P. T. Haertel, 2005: Zonal and vertical structure of the
675 Madden–Julian oscillation. *J. Atmos. Sci.*, 62, 2790–2809.

676 Kim, D., A. H. Sobel, E. D. Maloney, D. M. Frierson, and I.-S. Kang, 2011: A systematic
677 relationship between intraseasonal variability and mean state bias in AGCM simulations.
678 *J. Climate*, 24, 5506–5520.

679 Kim, D., I. S. Kug, and A. H. Sobel, 2014: Propagating versus nonpropagating Madden–Julian
680 oscillation events. *J. Climate*, 27, 111–125.

681 Kim, D., and Coauthors, 2009: Application of MJO simulation diagnostics to climate models. *J.*
682 *Climate*, 22, 6413–6436.

683 Kim, G.-U., and K.-H. Seo, 2017: Identifying a key physical factor sensitive to the performance
684 of Madden–Julian oscillation simulation in climate models. *Clim. Dyn.*, online published.

685 Klingaman, N. P., X. Jiang, P. K. Xavier, J. Petch, D. Waliser, and S. J. Woolnough, 2015:
686 Vertical structure and physical processes of the Madden-Julian oscillation: Synthesis and
687 summary. *J. Geophys. Res. Atmos.*, 120, 4671–4689.

688 Kuang, Z., 2008: A moisture-stratiform instability for convectively coupled waves. *J. Atmos.*

689 Sci., 65, 834–854.

690 Li, C. Y., X. L. Jia, J. Ling, W. Zhou, and C. D. Zhang, 2009: Sensitivity of MJO simulations to
691 diabatic heating profiles. *Clim. Dyn.*, 32, 167–187.

692 Ling, J., C. Zhang, S. Wang, and C. Li, 2017: A new interpretation of the ability of global
693 models to simulate the MJO. *Geophys. Res. Lett.*, 44, 5798–5806.

694 Madden, R. A., and P. R. Julian, 1972: Description of global-scale circulation cells in the tropics
695 with a 40–50 day period. *J. Atmos. Sci.*, 29, 1109–1123.

696 Mapes, B. E., 2000: Convective inhibition, subgrid-scale triggering energy, and stratiform
697 instability in a toy tropical wave model. *J. Atmos. Sci.*, 57, 1515–1535.

698 Merryfield, W. J., W.-S. Lee, G. J. Boer, V. V. Kharin, J. F. Scinocca, G. M. Flato, R. S.
699 Ajayamohan, J. C. Fyfe, Y. Tang, and S. Polavarapu, 2013: The Canadian seasonal to
700 interannual prediction system. Part I: Models and initialization. *Mon. Wea. Rev.*, 141,
701 2910–2945.

702 Maloney, E. D., 2009: The moist static energy budget of a composite tropical intraseasonal
703 oscillation in a climate model. *J. Climate*, 22, 711–729.

704 Maloney, E. D., and D. L. Hartmann, 1998: Frictional moisture convergence in a composite life
705 cycle of the Madden–Julian oscillation. *J. Climate*, 11, 2387–2403.

706 Maloney, E. D., A. H. Sobel, and W. M. Hannah, 2010: Intraseasonal variability in an aquaplanet
707 general circulation model. *J. Adv. Model. Earth Syst.*, 2, 1–14.

708 Molod, A., L. Takacs, L. M. Suarez, J. Bacmeister, I.-S. Song, and A. Eichmann, 2012: The
709 GEOS-5 atmospheric general circulation model: Mean climate and development from
710 MERRA to Fortuna, NASA Technical Report Series on Global Modeling and Data
711 Assimilation. NASATM-2012-104606, Vol. 28, 117 pp.

712 Neale, R. B., and Coauthors, 2012: Description of the NCAR Community Atmosphere Model:
713 CAM 5.0. Tech. Rep. NCAR/TN-486+STR, National Center for Atmospheric Research,
714 Boulder, Colorado.

715 Neena, J. M., D. Waliser, and X. Jiang, 2017: Model performance metrics and process
716 diagnostics for boreal summer intraseasonal variability. *Clim. Dyn.*, 48, 1661–1683.

717 Petch, J., D. Waliser, X. Jiang, P. Xavier, and S. Woolnough, 2011: A global model inter-
718 comparison of the physical processes associated with the MJO. *GEWEX News*, August.

719 Raymond, D. J., 2001: A new model of the Madden-Julian oscillation. *J. Atmos. Sci.*, 58, 2807-
720 2819.

721 Saha, S., and Coauthors 2006: The NCEP climate forecast system. *J. Climate*, 19, 3483–3517.

722 Saha, S., and Coauthors, 2013: The NCEP climate forecast system version 2. *J. Climate*, 27,
723 2185–2208.

724 Salby, M. L., H. H. Hendon, and R. R. Garcia, 1994: Planetary-scale circulations in the presence
725 of climatological and wave-induced heating. *J. Atmos. Sci.*, 51, 3365–3365.

726 Schmidt, G. A., and Coauthors, 2014: Configuration and assessment of the GISS ModelE2
727 contributions to the CMIP5 archive. *J. Adv. Model. Earth Syst.*, 6, 141–184.

728 Sobel, A., and E. Maloney, 2012: An idealized semi-empirical framework for modeling the
729 Madden–Julian oscillation. *J. Atmos. Sci.*, 69, 1691–1705.

730 Sobel, A., and E. Maloney, 2013: Moisture modes and the eastward propagation of the MJO. *J.*
731 *Atmos. Sci.*, 70, 187–192.

732 Song, X., and G. J. Zhang, 2011: Microphysics parameterization for convective clouds in a
733 global climate model: Description and single-column model tests. *J. Geophys. Res.*, 116,
734 D02201.

735 Sperber, K. R., 2003: Propagation and the vertical structure of the Madden-Julian oscillation.
736 Mon. Wea. Rev., 131, 3018–3037.

737 Sperber, K. R., and D. Kim, 2012: Simplified metrics for the identification of the Madden–Julian
738 oscillation in models. Atmos. Sci. Lett., 14, 187–193.

739 Stan, C., M. Khairoutdinov, C. A. DeMott, V. Krishnamurthy, D. M. Straus, D. A. Randall, J. L.
740 Kinter, and J. Shukla, 2010: An ocean-atmosphere climate simulation with an embedded
741 cloud resolving model. Geophys. Res. Lett., 37, L01702.

742 Stevens, B., and Coauthors, 2013: Atmospheric component of the MPI-M Earth System Model:
743 ECHAM6. J. Adv. Model. Earth Syst., 5, 146–172.

744 Tian, B. J., D. E. Waliser, E. Fetzer, B. Lambriksen, Y. Yung, and B. Wang, 2006: Vertical
745 moist thermodynamic structure and spatial-temporal evolution of the Madden-Julian
746 Oscillation in atmospheric infrared sounder observations. J. Atmos. Sci., 63, 2462-2485.

747 Tseng, W.-L., B.-J. Tsuang, N. Keenlyside, H.-H. Hsu, and C.-Y. Tu, 2014: Resolving the upper-
748 ocean warm layer improves the simulation of the Madden-Julian Oscillation. Clim. Dyn.,
749 44, 1487–1503.

750 Virts, K. S., and J. M. Wallace, 2010: Annual, interannual, and intraseasonal variability of
751 tropical tropopause transition layer cirrus. J. Atmos. Sci., 67, 3097–3112.

752 Virts, K. S., J. M. Wallace, Q. Fu, and T. P. Ackerman, 2010: Tropical tropopause transition
753 layer cirrus as represented by CALIPSO lidar observations. J. Atmos. Sci., 67, 3113-3129.

754 Voltaire, A., and Coauthors, 2013: The CNRM-CM5.1 global climate model: Description and
755 basic evaluation. Clim. Dyn., 40, 2091–2121.

756 Waliser, D. E., 2006: Intraseasonal variations. The Asian Monsoon, B. Wang, Ed., Springer,
757 203–257.

758 Waliser, D. E., M. W. Moncrieff, D. Burridge, A. H. Fink, D. Gochis, B. N. Goswami, B. Guan,
759 P. Harr, J. Heming, H.-H. Hsu, C. Jakob, M. Janiga, R. Johnson, S. Jones, P. Knippertz, J.
760 Marengo, H. Nguyen, M. Pope, Y. Serra, C. Thorncroft, M. Wheeler, R. Wood, and S.
761 Yuter, 2012: The “year” of tropical convection (May 2008–April 2010): Climate
762 variability and weather highlights. *Bull. Am. Meteorol. Soc.*, 93, 1189–1218.

763 Waliser, D. E., K. Sperber, H. Hendon, D. Kim, M. Wheeler, K. Weickmann, C. Zhang, et al.
764 2009: MJO simulation diagnostics. *J. Climate*, 22, 3006-3030.

765 Wang, B., 1988a: Comments on "An air-sea interaction model of intraseasonal oscillation in the
766 tropics". *J. Atmos. Sci.*, 45, 3521-3525.

767 Wang, B., 1988b: Dynamics of tropical low-frequency waves: An analysis of the moist Kelvin
768 wave. *J. Atmos. Sci.*, 45, 2051-2065.

769 Wang, B., and G. Chen, 2017: A general theoretical framework for understanding essential
770 dynamics of Madden-Julian Oscillation. *Clim. Dyn.*, 49, 2309–2328.

771 Wang, B., and H. Rui, 1990: Synoptic climatology of transient tropical intraseasonal convection
772 anomalies. *Meteor. Atmos. Phys.*, 44, 43-61.

773 Wang, B. and S.-S. Lee, 2017: MJO propagation shaped by zonal asymmetric structures: Results
774 from 24-GCM simulations. *J. Climate*, 30, 7933-7952.

775 Wang, B., and T. Li, 1994: Convective interaction with boundary-layer dynamics in the
776 development of a tropical intraseasonal system. *J. Atmos. Sci.*, 51, 1386–1400.

777 Wang, B., and X. Xie, 1997: A model for the boreal summer intraseasonal oscillation. *J. Atmos.*
778 *Sci.*, 54, 72-86.

779 Wang, B., F. Liu, and G. Chen, 2016: A trio-interaction theory for Madden-Julia Oscillation.
780 *Geoscience Letter*, 3, 34.

781 Watanabe, M., and Coauthors, 2010: Improved climate simulation by MIROC5: Mean states,
782 variability, and climate sensitivity. *J. Climate*, 23, 6312–6335.

783 Wheeler, M., and G. N. Kiladis, 1999: Convectively coupled equatorial waves: analysis of
784 clouds and temperature in the wavenumber-frequency domain. *J. Atmos. Sci.*, 56, 374–
785 399.

786 Wolding, B. O., and E. D. Maloney, 2015: Objective diagnostics and the Madden-Julian
787 Oscillation. Part II: Application to moist static energy and moisture budgets. *J.*
788 *Climate*, 28, 7786-7808.

789 Wu, T., R. Yu, F. Zhang, Z. Wang, M. Dong, L. Wang, X. Jin, D. Chen, and L. Li, 2010: The
790 Beijing Climate Center atmospheric general circulation model: Description and its
791 performance for the present-day climate. *Clim. Dyn.*, 34, 123–147.

792 Wu, X., and L. Deng, 2013: Comparison of moist static energy and budget between the GCM-
793 simulated Madden-Julian oscillation and observations over the Indian Ocean and western
794 Pacific. *J. Climate*, 26, 4981–4993.

795 Yanai, M., S. Esbensen, and J.-H. Chu, 1973: Determination of bulk properties of tropical cloud
796 clusters from large-scale heat and moisture budgets. *J. Atmos. Sci.*, 30, 611–627.

797 Yoneyama, K., C. Zhang, and C. N. Long, 2013: Tracking pulses of the Madden-Julian
798 Oscillation. *Bull. Amer. Met. Soc.*, 94, 1871-1891.

799 Yukimoto, S., and Coauthors, 2012: A new global climate model of the Meteorological Research
800 Institute: MRI-CGCM3 - Model description and basic performance -. *J. Meteorol. Soc.*
801 *Jpn. Ser. II*, 90A, 23-64.

802 Zhang, C., 2005: Madden-Julian Oscillation. *Rev. Geophys.*, 43, RG2003.

803 Zhang, C., 2013: Madden-Julian Oscillation: Bridging weather and climate. *Bull. Amer. Meteor.*

804 Soc., 94, 1849-1870.

805 Zhang, C., and J. Ling, 2017: Barrier effect of the Indo-Pacific Maritime Continent on the MJO:
806 Perspectives from tracking MJO precipitation. *J. Climate*, 30, 3439–3459.

807 Zhang, G. J., and M. Mu, 2005: Simulation of the Madden-Julian oscillation in the NCAR
808 CCM3 using a revised Zhang-McFarlane convection parameterization scheme. *J. Climate*,
809 18, 4046–4064.

810 Zhang, G., and X. L. Song, 2009: Interaction of deep and shallow convection is key to Madden–
811 Julian Oscillation simulation. *Geophys. Res. Lett.*, 36, L09708.

812 Zhu, H., and H. Hendon, 2015: Role of large scale moisture advection for simulation of the MJO
813 with increased entrainment. *Quart. J. Roy Met. Soc.*, 141, 2127–2136.

814 Zhu, H., H. Hendon, and C. Jacob, 2009: Convection in a parameterized and super-parameterized
815 model and its role in the representation of the MJO. *J. Atmos. Sci.*, 66, 2796-2811.

816

817

818

819

820

821

822

823

824

825

826

827 **Table and Figure captions**

828 **Table 1** List of the models participating in the 20-year climate simulations

829 **Table 2.** The dynamics-oriented diagnostics for the intrinsic mode of MJO.

830 **Table 3.** Summary of 24 models' performances in simulation of the dynamics-oriented
831 diagnostics. The model groups are determined based on the PCCs of the eastward
832 propagation of precipitation between the observation and model simulations (Fig. 1d).
833 The number in the Table indicates an averaged PCC skill for each model group between
834 the observation and corresponding simulation.

835

836 **Fig. 1** Eastward propagation of MJO precipitation as indicated by the lead-lag correlation of 20-
837 70 day filtered precipitation averaged over 10°S-10°N with reference to the precipitation
838 at the equatorial eastern Indian Ocean (10°S-10°N, 80°-100°E) during boreal winter
839 (NDJFMA): (a) Observation, (b) excellent model (top 6 models in d) composite, and (c)
840 poor model (poorest 6 models in d) composite. The red contour represents correlation
841 coefficient (CC) of ± 0.2 . Black dotted lines indicate eastward propagation speed of 5 m s⁻¹.
842 (d) Pattern correlation coefficients (PCCs) of the eastward propagation of precipitation
843 between the observation and model simulations. The PCC skill is calculated in the time-
844 longitude domain (50°-180°E, from day -20 to day 20, the blue rectangle in a) where the
845 magnitude of the observed CC exceeds 0.2 and the longitude range between 85°E and
846 95°E is excluded.

847 **Fig. 2** Boundary layer moisture convergence and its zonal asymmetry. (a) Observed structure
848 shown by the regressed 20-70 day filtered 925-hPa moisture convergence (BLMC) (day⁻¹)
849 onto the 20-70 day filtered precipitation at the equatorial eastern Indian Ocean (10°S-

850 10°N, 80°-100°E), which is symbolized by the black filled circle. (b) Longitudinal
851 variations of the BLMC averaged between 5°S and 5°N in observation, composite of
852 excellent models, and composite of poor models, respectively. (c) The relationship
853 between MJO eastward propagation skill and BLMC structure skill. The regressed
854 strength in (a) and (b) is scaled to a fixed 3 mm day⁻¹ precipitation rate at the MJO
855 precipitation center. The regressed fields in (b) are normalized by their minimum values.
856 The MJO eastward propagation skill in (c) indicates the PCC score in Fig. 1(d). The PCC
857 skill for BLMC in (c) is calculated over 15°S-15°N, 50°-160°E (black rectangle in a).

858 **Fig. 3** Propagation of precluding boundary layer moisture convergence (BLMC). (a) Lead-lag
859 regressed 20-70 day filtered BLMC (day⁻¹, shading) onto the 20-70 day filtered
860 precipitation at the equatorial eastern Indian Ocean (10°S-10°N, 80°-100°E). The
861 regressed strength is scaled to a fixed 3 mm day⁻¹ precipitation rate and averaged over
862 5°S-5°N. For comparison, the eastward propagation of precipitation shown in Fig. 1(a)
863 also plotted as contours (CI=0.2). (b) The relationship between MJO eastward
864 propagation skill (in Fig. 1d) and BLMC propagation skill, which is measured by the
865 PCC between the observed and simulated BLMC propagation maps on the time-longitude
866 domain (50°-180°E, from day -20 to day +20). The longitude range between 85°E and
867 95°E is excluded in the calculation of PCC. The thick blue and black lines in (a) indicate
868 the maximum regression coefficient of BLMC and maximum correlation coefficient of
869 precipitation, respectively.

870 **Fig. 4** Zonal asymmetry in the low-level circulation. (a) Observed structures of 850 hPa winds
871 (m s⁻¹, vector) and zonal wind speed (U850) (m s⁻¹, shading). (b) Comparison of the
872 longitudinal variations of the U850 in observation, composite of excellent models, and

873 composite of poor models. (c) The relationship between MJO eastward propagation skill
874 and the PCC skill for U850 structure. (d) Same as in (c) but for U850 asymmetric index,
875 which is defined as the ratio of the maximum Kelvin easterly speed vs. the maximum
876 Rossby westerly speed, both are averaged between 5°S and 5°N. The black filled circle
877 represents observation. The structures in panel (a) and (b) are reconstructed using the
878 same methods as used in Fig. 2(a) and 2(b), respectively. The regressed fields in (b) are
879 normalized by their maximum values. The skills in panel (c) and (d) are computed using
880 the same method as used in Fig. 2(c).

881 **Fig. 5** Zonal asymmetry in MJO thermal structure. (a) Observed vertical structures of equivalent
882 potential temperature (EPT) (K, shading) and specific humidity (g kg^{-1} , black contour,
883 $\text{CI}=0.1$) averaged between 5°S-5°N, which are the regressed 20-70 day filtered fields onto
884 20-70 day filtered precipitation at the equatorial eastern Indian Ocean (10°S-10°N, 80°-
885 100°E). The regressed strengths are scaled to a fixed 3 mm day^{-1} precipitation rate. The
886 black line shows titled axis of the EPT maximum. (b) Longitudinal variations of the
887 EPT850-EPT400 (convective instability index). The regressed fields are normalized by
888 their minimum values. The orange vertical lines indicate the longitude range where the
889 convective instability index in (d) is calculated. (c) The relationship between MJO
890 eastward propagation skill and the PCC skill (40°-180°E, 1000-200 hPa) for vertical
891 structure of EPT. (d) Same as (c) but for convective instability index. The black filled
892 circle in (d) represents observation. The skills in panel (c) and (d) are computed using the
893 same method as used in Fig. 2(c).

894 **Fig. 6** Zonal asymmetry in diabatic heating (K day^{-1} , shading) and anomalous Walker cell (m s^{-1}
895 for zonal wind and 0.01 Pa s^{-1} for vertical velocity, vector) averaged between 5°S-5°N in

896 (a) observation, (b) excellent model composite, and (c) poor model composite. (d) The
897 relationship between MJO eastward propagation skill and PCC skill for vertical structure
898 of diabatic heating. The structures in panel (a), (b), and (c) are reconstructed using the
899 same method as used in Fig. 5(a). The skills in panel (d) are computed using the same
900 method as used in Fig. 2(c).

901 **Fig. 7** The 200 hPa wind (m s^{-1} , vector), divergence (day^{-1} , contour), and the 300 hPa diabatic
902 heating (K day^{-1} , shading) in (a) observation, (b) excellent model composite, and (c) poor
903 model composite. Panel (d) and (e) show the relationship between MJO propagation skill
904 and the PCC skill for (d) 200 hPa divergence and (e) 300 hPa diabatic heating. The
905 structures in panel (a), (b), and (c) are reconstructed using the same method as used in Fig.
906 2(a). The skills in panel (d) and (e) are computed using the same method as used in Fig.
907 2(c).

908 **Fig. 8** (a) Eddy available potential energy (APE) generation rate ($\text{K}^2 \text{ day}^{-1}$, contour) and
909 temperature anomalies (K, shading) averaged between 5°S - 5°N . (b) The relationship
910 between MJO propagation skill and PCC skill for vertical structure of APE. The
911 structures in panel (a) and the skills in panel (b) are compute using the same methods as
912 used in Fig. 5(a) and Fig. 2(c), respectively.

913

914

915

916

917

918

919

920

921 **Table 1** A list of models participating in the 20-year climate simulations.

Model name	Institute	References
ACCESS1	Centre for Australian Weather and Climate Research	Zhu and Hendon (2015)
BCC-AGCM	Beijing Climate Center, China Meteorological Administration	Wu et al. (2010]
CAM5	National Center for Atmospheric Research	Neale et al. (2012)
CAM5-ZM	Lawrence Livermore National Laboratory	Song and Zhang (2011]
CanCM4	Canadian Centre for Climate Modelling and Analysis	Merryfield et al. (2013)
CFS2	Climate Prediction Center, NCEP/NOAA	Saha et al. (2013)
CNRM-AM	Centre National de la Recherche Scientifique/Météo-France	Voltaire et al. (2013)
CNRM-CM		
CNRM-ACM		
ECEarth3	Rosby Centre, Swedish Meteorological and Hydrological Institute	Batté and Doblas-Reyes (2015)
EC-GEM	Environment Canada	Côté et al. (1998)
ECHAM5-SIT	Academia Sinica, Taiwan	Tseng et al. (2014)
ECHAM6	Max Planck Institute for Meteorology	Stevens et al. (2013)
FGOALS-s2	Institute of Atmospheric Physics, Chinese Academy of Sciences	Bao et al. (2013)
GEOS5	Global Modeling and Assimilation Office, NASA	Molod et al. (2012)
GISS-S2	Goddard Institute for Space Studies, NASA	Schmidt et al. (2014)
ISUGCM	Iowa State University	Wu and Deng (2013)
MIROC5	AORI/NIES/JAMSREC, Japan	Watanabe et al. (2010)
MRI-AGCM	Meteorological Research Institute, Japan	Yukimoto et al. (2012)
NavGEM1	US Naval Research Laboratory	Hogan et al. (2014)
PNU-CFS	Pusan National University	Saha et al. (2006)
SPCAM3	Colorado State University	Khairoutdinov et al. (2008)
SPCCSM3	George Mason University	Stan et al. (2010)
UCSD-CAM3	Scripps Institute of Oceanography	Zhang and Mu (2005)

922

923

924

925

926 **Table 2.** The dynamics-oriented diagnostics for the intrinsic mode of MJO.

Dynamical process	Diagnostic fields	PCC with MJO precipitation propagation
1. Boundary layer moisture convergence (BLMC) leads convection	Horizontal structure of 925 hPa moisture convergence	0.79 (Fig. 2c)
2. Precluding eastward propagation of BLMC	Lag-longitude regression of 925 hPa moisture convergence	0.83 (Fig.3b)
3. Zonal asymmetry in the low-level circulation: Kelvin easterly vs Rossby westerly	U850 structure and zonal asymmetry index along the equator (Maximum Kelvin easterly vs. maximum Rossby westerly)	0.74 (Fig. 4c)
4. Deepening of the lower tropospheric moist layer and destabilization ahead of convection	Zonal-vertical structure of EPT and convective instability index (EPT 850 hPa minus EPT 400 hPa to the east of MJO)	0.77 (Fig. 5c)
5. Multi-cloud structure: Transition from shallow - congestus to deep convective clouds	Vertical structure of diabatic heating (and Walker cell) along the equator	0.86 (Fig. 6d)
6. Zonal asymmetry in the upper level divergence and the role of stratiform clouds	Horizontal structure of 200 hPa divergence and 300 hPa diabatic heating	0.75 (Fig. 7d)
7. Amplification and propagation of MJO	Vertical structure of available potential energy generation along the equator	0.84 (Fig. 8b)

927

928

929

930

931

932

933

934

935 **Table 3.** Summary of 24 models’ performances in simulation of the dynamics-oriented
 936 diagnostics. The model groups are determined based on the PCCs of the eastward
 937 propagation of precipitation between the observation and model simulations (Fig. 1d).
 938 The number in the Table indicates an averaged PCC skill for each model group between
 939 the observation and corresponding simulation.

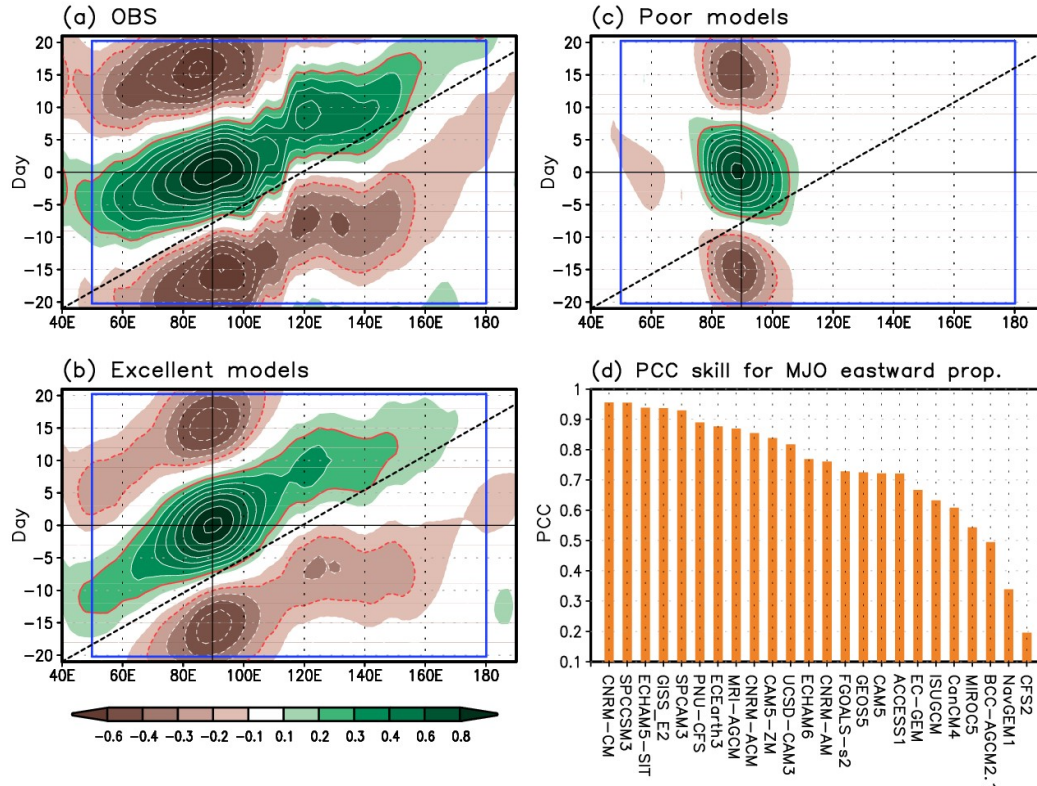
Diagnostic fields	Model groups (Fig. 1d)			
	Excellent	Good	Fair	Poor
Horizontal structure of BLMC	0.68	0.61	0.54	0.45
Propagation of BLMC	0.84	0.68	0.63	0.40
Horizontal structure of U850	0.89	0.84	0.73	0.69
Vertical structure of EPT	0.86	0.81	0.78	0.66
Vertical structure of diabatic heating	0.89	0.83	0.80	0.64
Horizontal structure of 200 hPa divergence	0.86	0.81	0.76	0.68
Vertical structure of eddy APE generation	0.90	0.81	0.78	0.62

940

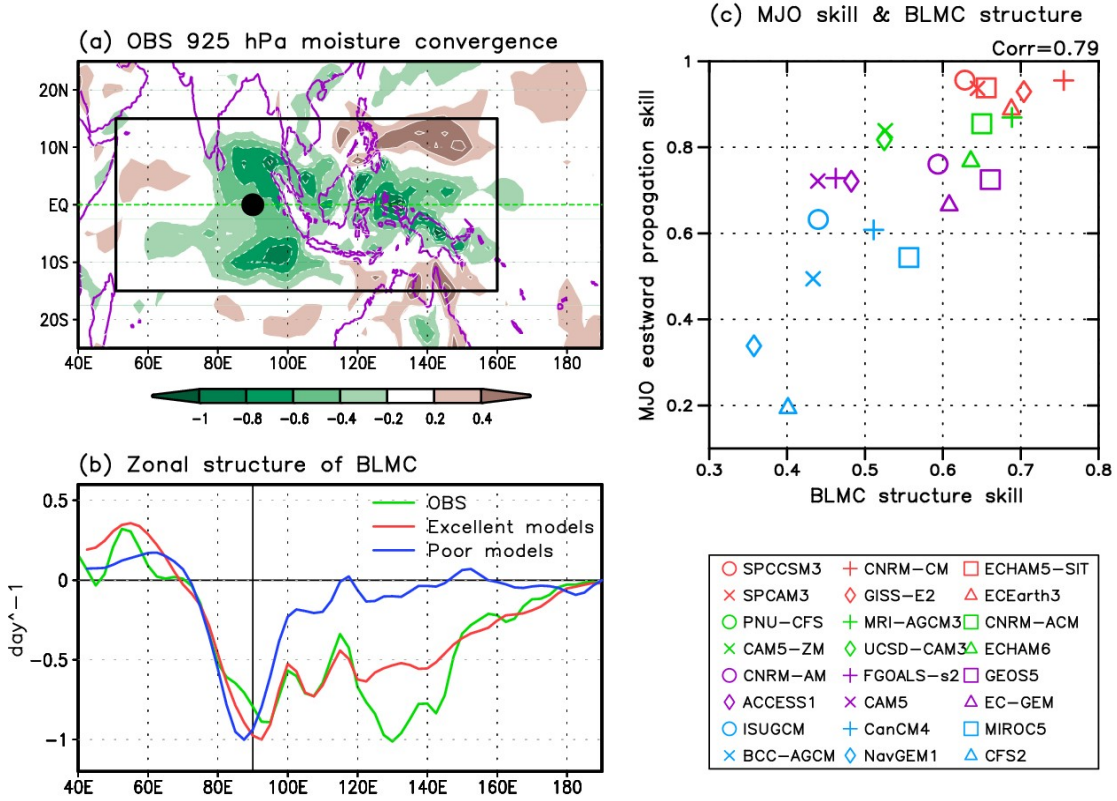
941

942

943



944
 945 **Fig. 1** Eastward propagation of MJO precipitation as indicated by the lead-lag correlation of 20-
 946 70 day filtered precipitation averaged over 10°S-10°N with reference to the precipitation
 947 at the equatorial eastern Indian Ocean (10°S-10°N, 80°-100°E) during boreal winter
 948 (NDJFMA): (a) Observation, (b) excellent model (top 6 models in d) composite, and (c)
 949 poor model (poorest 6 models in d) composite. The red contour represents correlation
 950 coefficient (CC) of ±0.2. Black dotted lines indicate eastward propagation speed of 5 m s⁻¹.
 951 (d) Pattern correlation coefficients (PCCs) of the eastward propagation of precipitation
 952 between the observation and model simulations. The PCC skill is calculated in the time-
 953 longitude domain (50°-180°E, from day -20 to day 20, the blue rectangle in a) where the
 954 magnitude of the observed CC exceeds 0.2 and the longitude range between 85°E and
 955 95°E is excluded.
 956



957

958

Fig. 2 Boundary layer moisture convergence and its zonal asymmetry. (a) Observed structure

959

shown by the regressed 20-70 day filtered 925-hPa moisture convergence (BLMC) (day^{-1})

960

onto the 20-70 day filtered precipitation at the equatorial eastern Indian Ocean (10°S -

961

10°N , 80° - 100°E), which is symbolized by the black filled circle. (b) Longitudinal

962

variations of the BLMC averaged between 5°S and 5°N in observation, composite of

963

excellent models, and composite of poor models, respectively. (c) The relationship

964

between MJO eastward propagation skill and BLMC structure skill. The regressed

965

strength in (a) and (b) is scaled to a fixed 3 mm day^{-1} precipitation rate at the MJO

966

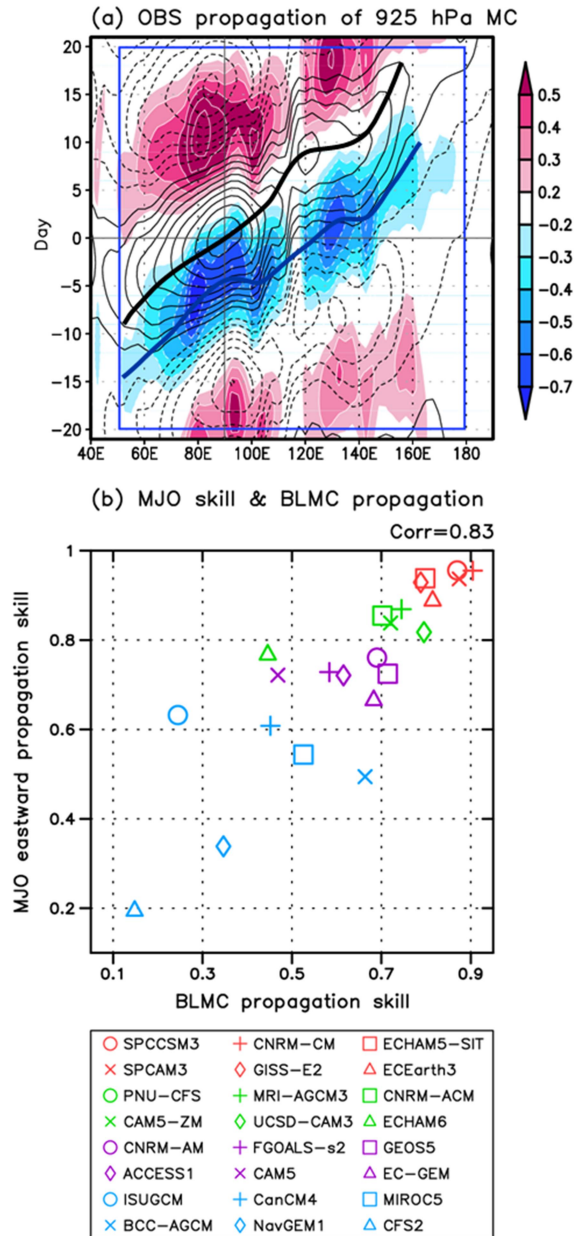
precipitation center. The regressed fields in (b) are normalized by their minimum values.

967

The MJO eastward propagation skill in (c) indicates the PCC score in Fig. 1(d). The PCC

968

skill for BLMC in (c) is calculated over 15°S - 15°N , 50° - 160°E (black rectangle in a).



969

970 **Fig. 3** Propagation of precluding boundary layer moisture convergence (BLMC). (a) Lead-lag
 971 regressed 20-70 day filtered BLMC (day^{-1} , shading) onto the 20-70 day filtered
 972 precipitation at the equatorial eastern Indian Ocean ($10^{\circ}\text{S}-10^{\circ}\text{N}$, $80^{\circ}-100^{\circ}\text{E}$). The
 973 regressed strength is scaled to a fixed 3 mm day^{-1} precipitation rate and averaged over
 974 $5^{\circ}\text{S}-5^{\circ}\text{N}$. For comparison, the eastward propagation of precipitation shown in Fig. 1(a)

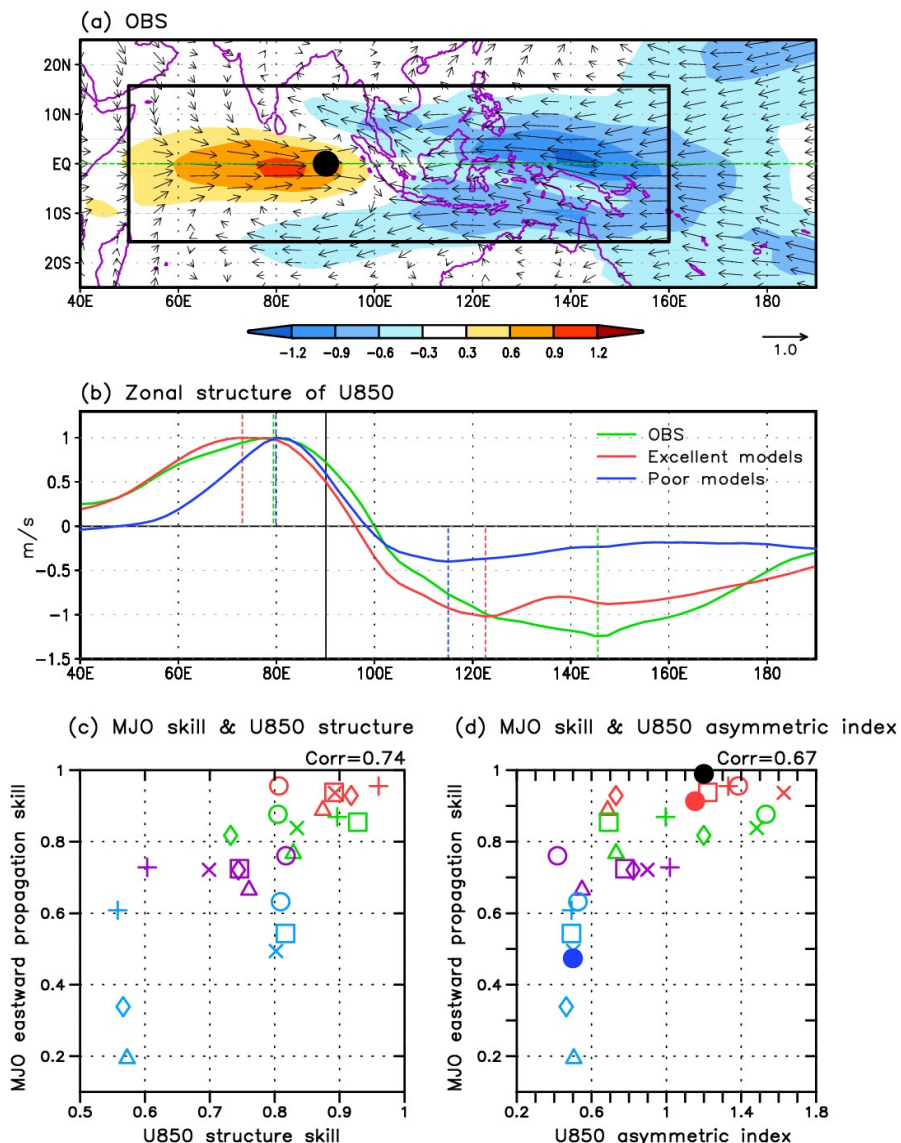
975 also plotted as contours (CI=0.2). (b) The relationship between MJO eastward
976 propagation skill (in Fig. 1d) and BLMC propagation skill, which is measured by the
977 PCC between the observed and simulated BLMC propagation maps on the time-longitude
978 domain (50°-180°E, from day -20 to day +20). The longitude range between 85°E and
979 95°E is excluded in the calculation of PCC. The thick blue and black lines in (a) indicate
980 the maximum regression coefficient of BLMC and maximum correlation coefficient of
981 precipitation, respectively.

982

983

984

850 hPa zonal wind speed and circulation



985
 986 **Fig. 4** Zonal asymmetry in the low-level circulation. (a) Observed structures of 850 hPa winds
 987 (m s^{-1} , vector) and zonal wind speed (U850) (m s^{-1} , shading). (b) Comparison of the
 988 longitudinal variations of the U850 in observation, composite of excellent models, and
 989 composite of poor models. (c) The relationship between MJO eastward propagation skill
 990 and the PCC skill for U850 structure. (d) Same as in (c) but for U850 asymmetric index,
 991 which is defined as the ratio of the maximum Kelvin easterly speed vs. the maximum

992 Rossby westerly speed, both are averaged between 5°S and 5°N. The black filled circle
993 represents observation. The structures in panel (a) and (b) are reconstructed using the
994 same methods as used in Fig. 2(a) and 2(b), respectively. The regressed fields in (b) are
995 normalized by their maximum values. The skills in panel (c) and (d) are computed using
996 the same method as used in Fig. 2(c).

997

998

999

1000

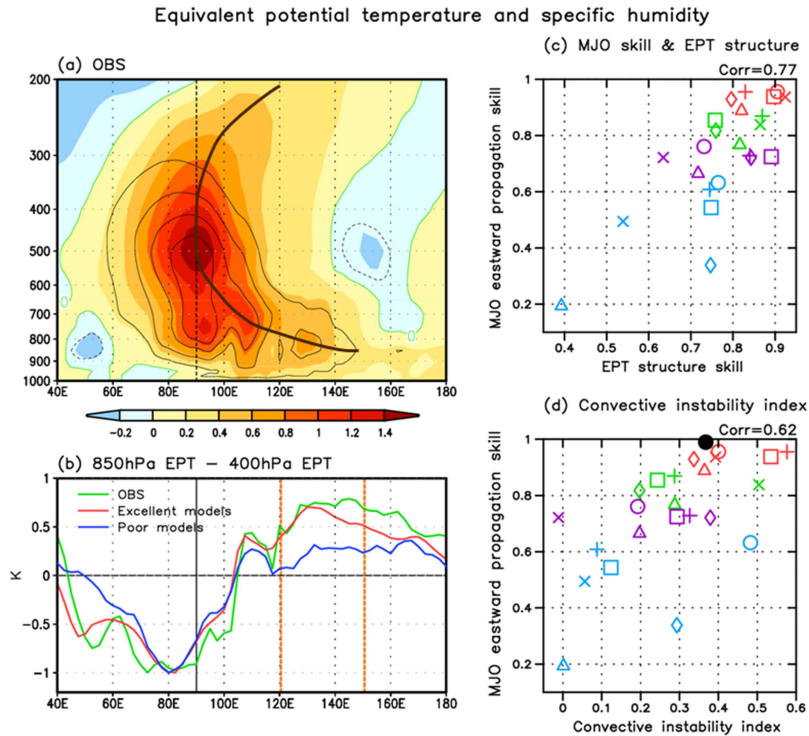
1001

1002

1003

1004

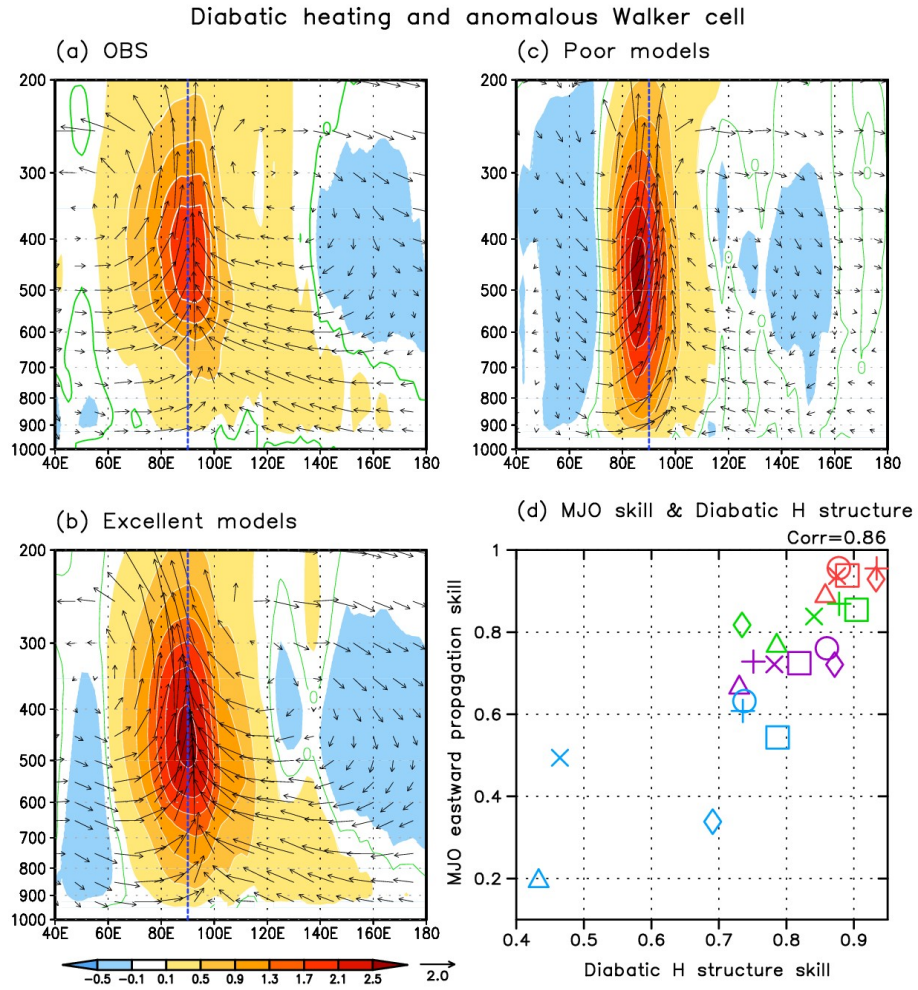
1005



1006

1007 **Fig. 5** Zonal asymmetry in MJO thermal structure. (a) Observed vertical structures of equivalent
 1008 potential temperature (EPT) (K, shading) and specific humidity (g kg^{-1} , black contour,
 1009 $\text{CI}=0.1$) averaged between 5°S - 5°N , which are the regressed 20-70 day filtered fields onto
 1010 20-70 day filtered precipitation at the equatorial eastern Indian Ocean (10°S - 10°N , 80° -
 1011 100°E). The regressed strengths are scaled to a fixed 3 mm day^{-1} precipitation rate. The
 1012 black line shows titled axis of the EPT maximum. (b) Longitudinal variations of the
 1013 EPT_{850} - EPT_{400} (convective instability index). The regressed fields are normalized by
 1014 their minimum values. The orange vertical lines indicate the longitude range where the
 1015 convective instability index in (d) is calculated. (c) The relationship between MJO
 1016 eastward propagation skill and the PCC skill (40° - 180°E , 1000-200 hPa) for vertical
 1017 structure of EPT. (d) Same as (c) but for convective instability index. The black filled
 1018 circle in (d) represents observation. The skills in panel (c) and (d) are computed using the
 1019 same method as used in Fig. 2(c).

1020



1021

1022 **Fig. 6** Zonal asymmetry in diabatic heating (K day^{-1} , shading) and anomalous Walker cell (m s^{-1}

1023 for zonal wind and 0.01 Pa s^{-1} for vertical velocity, vector) averaged between 5°S - 5°N in

1024 (a) observation, (b) excellent model composite, and (c) poor model composite. (d) The

1025 relationship between MJO eastward propagation skill and PCC skill for vertical structure

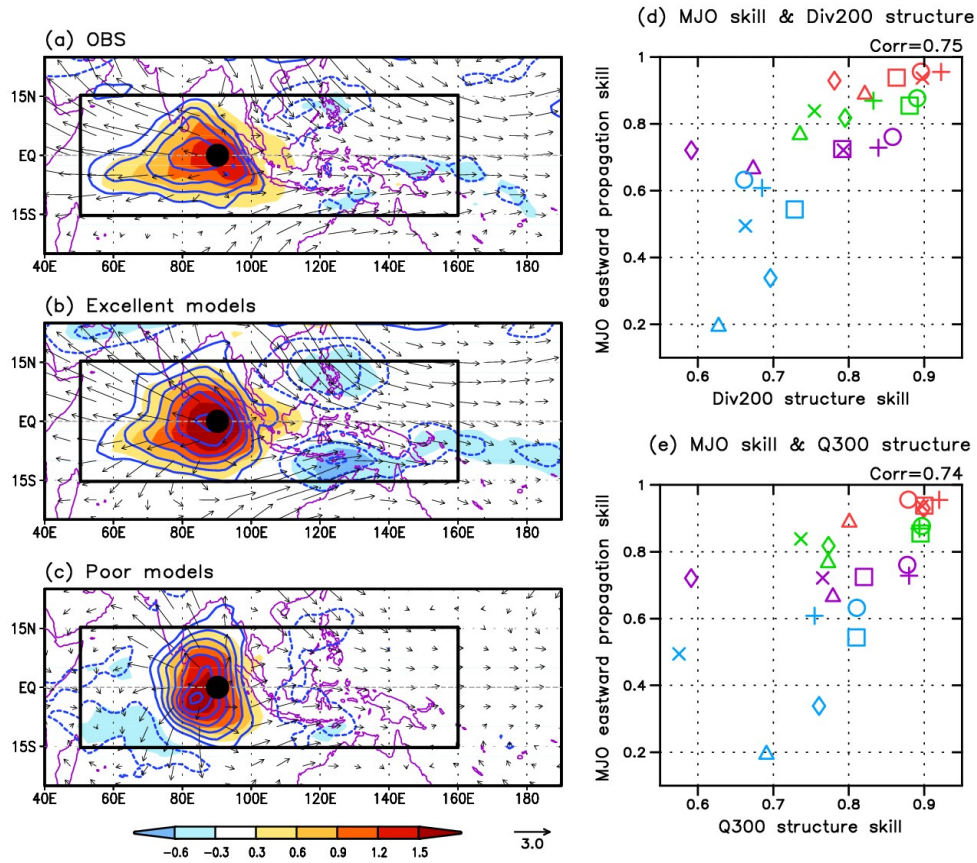
1026 of diabatic heating. The structures in panel (a), (b), and (c) are reconstructed using the

1027 same method as used in Fig. 5(a). The skills in panel (d) are computed using the same

1028 method as used in Fig. 2(c).

1029

200 hPa divergence and 300 hPa diabatic heating

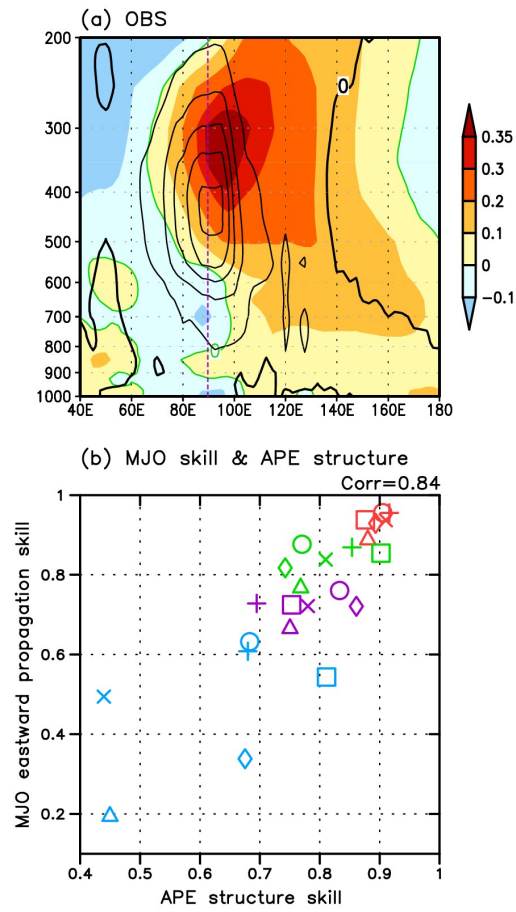


1030

1031 **Fig. 7** The 200 hPa wind (m s^{-1} , vector), divergence (day^{-1} , contour), and the 300 hPa diabatic
 1032 heating (K day^{-1} , shading) in (a) observation, (b) excellent model composite, and (c) poor
 1033 model composite. Panel (d) and (e) show the relationship between MJO propagation skill
 1034 and the PCC skill for (d) 200 hPa divergence and (e) 300 hPa diabatic heating. The
 1035 structures in panel (a), (b), and (c) are reconstructed using the same method as used in Fig.
 1036 2(a). The skills in panel (d) and (e) are computed using the same method as used in Fig.
 1037 2(c).

1038

Available Potential Energy generation rate



1039

1040 **Fig. 8** (a) Eddy available potential energy (APE) generation rate ($K^2 \text{ day}^{-1}$, contour) and
 1041 temperature anomalies (K, shading) averaged between 5°S - 5°N . (b) The relationship
 1042 between MJO propagation skill and PCC skill for vertical structure of APE. The
 1043 structures in panel (a) and the skills in panel (b) are compute using the same methods as
 1044 used in Fig. 5(a) and Fig. 2(c), respectively.

1045